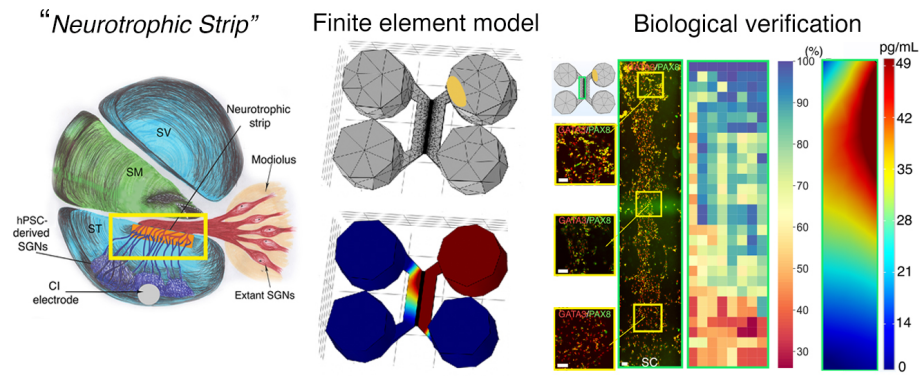


# Graphical Abstract

## Developing the Bioactive Cochlear Implant: Bridging the electrode–neuron gap through neurite guidance

Kevin T. Nella, Benjamin M. Norton, Hsiang-Tsun Chang, Rachel A. Heuer,  
Christian B. Roque, Akihiro J. Matsuoka



# Developing the Bioactive Cochlear Implant: Bridging the electrode–neuron gap through neurite guidance

Kevin T. Nella<sup>a,b</sup>, Benjamin M. Norton<sup>a</sup>, Hsiang-Tsun Chang<sup>a</sup>, Rachel A. Heuer<sup>a</sup>, Christian B. Roque<sup>a</sup>, Akihiro J. Matsuoka<sup>a,c,d,e,\*</sup>

<sup>a</sup>*Department of Otolaryngology–Head and Neck Surgery, Feinberg School of Medicine, Northwestern University, Chicago IL, 60611, USA*

<sup>b</sup>*Department of Mechanical Engineering, Robert R. McCormick School of Engineering and Applied Science, Northwestern University, Evanston, IL., USA*

<sup>c</sup>*Simpson Querrey Institute, Chicago IL, 60611, USA*

<sup>d</sup>*Roxelyn and Richard Pepper Department of Communication Sciences and Disorders, School of Communication, Northwestern University, Evanston, IL., 60210, USA*

<sup>e</sup>*The Hugh Knowles Center for Clinical and Basic Science in Hearing and its Disorders, Evanston, IL. 60210, USA*

---

## Abstract

Although cochlear implant (CI) technology has allowed partial restoration of hearing over the last few decades, persistent challenges remain - including the deciphering of rich acoustic signals into a digital pulse-train signal. Among these challenges, the “electrode–neuron gap” poses the most significant obstacle to advancing past the current plateau in CI performance. Resulting issues include limited performance in noisy environments and a poor ability to decode intonation and music. We propose the development of a “neurotrophic strip”—a biological interface that doubly preserves endogenous spiral ganglion neurons (SGNs) while precisely directing the growth of neurites arising from transplanted human pluripotent stem cell (hPSC)-derived otic neuronal progenitors (ONPS), toward endogenous SGNs. We hypothesized that the Polyhedrin Delivery System (PODS®-human brain-derived neurotrophic factor [BDNF]) could stably

---

\*Corresponding author: Akihiro J. Matsuoka, Department of Otolaryngology–Head and Neck Surgery, Feinberg School of Medicine, Northwestern University, 676 North St. Clair Street Suite 1325, Chicago, IL 60611, USA. E-mail addresses: amatsuok@nm.org, akihiro.matsuoka@northwestern.edu.

Email addresses: kevin.nella@northwestern.edu (Kevin T. Nella), benjamin.norton@northwestern.edu (Benjamin M. Norton), hsiangtsun.chang@gmail.com (Hsiang-Tsun Chang), racheuer@gmail.com (Rachel A. Heuer), christian.b.roq@gmail.com (Christian B. Roque), amatsuok@nm.org (Akihiro J. Matsuoka)

provide an adequate BDNF gradient to hPSC-derived ONPs, thereby simultaneously facilitating otic neuronal differentiation and directional neurite outgrowth. To test this hypothesis, we first devised a finite element model to simulate the *in vitro* BDNF gradient generated by PODS®. For biological verification, we validated the concept of the neurotrophic strip by using a multi-chamber microfluidic device, which mimics the *in vivo* micro-environment more accurately than conventional laboratory plates in terms of volume and concentrations of endogenous/exogenous factors. We were able to generate the optimal BDNF concentration gradient to enable survival, neuronal differentiation toward hPSC-derived SGNs, and directed neurite extension of hPSC-derived SGNs. The technique will allow us to further advance our concept of the “neurotrophic strip” by controlling neurite direction of transplanted hPSC-derived ONPs. This proof-of-concept study provides a step toward the next generation of CI technology.

*Keywords:* human pluripotent stem cells, finite element model, microfluidic device, neurotrophic factor, cochlear implant, neuroelectric interface, stem cell niche, spiral ganglion neurons

*2010 MSC:* 74S05, 62P10, 92C20

---

<sup>1</sup> **1. Introduction**

<sup>2</sup> The cochlear implant (CI), which provides functional restoration in patients  
<sup>3</sup> with sensorineural hearing loss, forms a neuro-electronic interface with the pe-  
<sup>4</sup> ripheral auditory nervous system [1]. CI technology functions by electrically  
<sup>5</sup> stimulating the extant population of auditory neurons (i.e., spiral ganglion neu-  
<sup>6</sup> rons [SGNs]). Although CI technology has allowed partial restoration of hearing  
<sup>7</sup> for this patient population over the last few decades, persistent challenges, in-  
<sup>8</sup> cluding the deciphering of rich acoustic signals into digital pulse-train signals,  
<sup>9</sup> remain. Among these challenges, the “electrode-neuron gap” poses the most  
<sup>10</sup> significant obstacle to advancing past the current plateau in CI performance.  
<sup>11</sup> This phenomenon results in limited performance in noisy environments and poor  
<sup>12</sup> ability to decode intonation and music [2], arguably decreasing quality of life.  
<sup>13</sup> The gap exists between the CI electrode and the target membranes of dendrites  
<sup>14</sup> in surviving endogenous SGNs [3]. It results in the requirement of larger CI  
<sup>15</sup> excitation fields, leading to current spread that excites and therefore disables  
<sup>16</sup> the neighboring electrodes, resulting in fewer information channels to the brain,  
<sup>17</sup> all within discrete time steps [2, 4]. This can develop into a vicious cycle as  
<sup>18</sup> fewer information channels to the brain also prompt the need for larger CI ex-  
<sup>19</sup> citation fields. The length of the gap generally spans hundreds of  $\mu\text{m}$  [5, 6].  
<sup>20</sup> Hahnewald et al. demonstrated *in vitro* that energy needed to elicit a response  
<sup>21</sup> can be reduced by up to 20% by reducing the distance from 40 to zero  $\mu\text{m}$  (by  
<sup>22</sup> growing early postnatal mouse SGN explants on a microelectrode array) [4].

<sup>23</sup> To resolve the electrode-neuron gap *in vivo*, previous work has introduced  
<sup>24</sup> the concept of a bioactive CI (Figure. 1A) [7, 8, 9]. The bioactive CI combines  
<sup>25</sup> the current state-of-the-art CI technology with emerging stem cell-replacement  
<sup>26</sup> therapy in the inner ear. In this scheme, transplanted human pluripotent stem  
<sup>27</sup> cell (hPSC)-derived SGNs bridge the gap between the CI electrode and sur-  
<sup>28</sup> viving endogenous SGNs. Neurotrophin gradients have been shown to guide  
<sup>29</sup> hPSC grafts in spinal cord injury [10], direct growth of endogenous SGNs to-  
<sup>30</sup> ward CI electrodes in the scala tympani [11], and enable transplanted hPSC

31 derived otic neuronal progenitors (ONPs) to grow neurites toward the modiolus  
32 [9]. Although promising, these studies failed to observe adequate directional  
33 neurite outgrowth toward endogenous SGNs (i.e., lack of synaptic connections  
34 between hPSC grafts and endogenous SGNs), presumably preventing significant  
35 improvements in functional recovery of hearing.

36 To confront this issue, we propose the development of a “neurotrophic strip”—a  
37 biological interface that doubly preserves endogenous SGNs while precisely di-  
38 recting the growth of neurites arising from transplanted hPSC-derived ONPs  
39 toward the endogenous SGNs. The highlighted yellow-square area in Figure  
40 1A shows a schematic diagram of this concept. Here, the neurotrophic strip  
41 (shown as an orange rectangle in Figure 1A) stimulates neurite outgrowth from  
42 both the hPSC-derived ONPs and the endogenous SGNs via a neurotrophic fac-  
43 tor gradient [12]. While the concept of a neurotrophin gradient for directional  
44 axonal growth has existed for a few decades, incorporating neurotrophin gradi-  
45 ents into any tissue-engineered scaffold has been extremely challenging due to  
46 the lack of self-sustaining neurotrophin delivery methods—their eventual deple-  
47 tion triggers an accelerated decline in neurite growth and the survival of extant  
48 SGNs [13, 14, 15]. One major contributor is the structurally unstable nature of  
49 neurotrophins, which suffer from fragility and thermo-instability under normal  
50 physiological conditions both *in vitro* and *in vivo*, leading to short half-lives typi-  
51 cally ranging from minutes to hours [16]. This issue can be overcome by utilizing  
52 the polyhedrin delivery system (PODS®)—a crystalline growth factor formu-  
53 lation developed to enable long-term release of growth factors while dampening  
54 degradation rates at the source [17, 18, 19] (Figure 1B). The PODS® technology  
55 has adapted viral machinery to encase a chosen growth factor into polyhedrin  
56 protein cases. The resultant growth factor co-crystals have slow degradation pro-  
57 files under physiological conditions and, therefore, allow the sustained release of  
58 embedded bioactive growth factor protein such as neurotrophins.

59 We reasoned that an bio-engineered scaffolding incorporated with PODS®  
60 technology can establish a neuronal network between transplanted hPSC-derived  
61 ONP grafts and extant SGNs in the inner ear. More specifically, we hypothesized

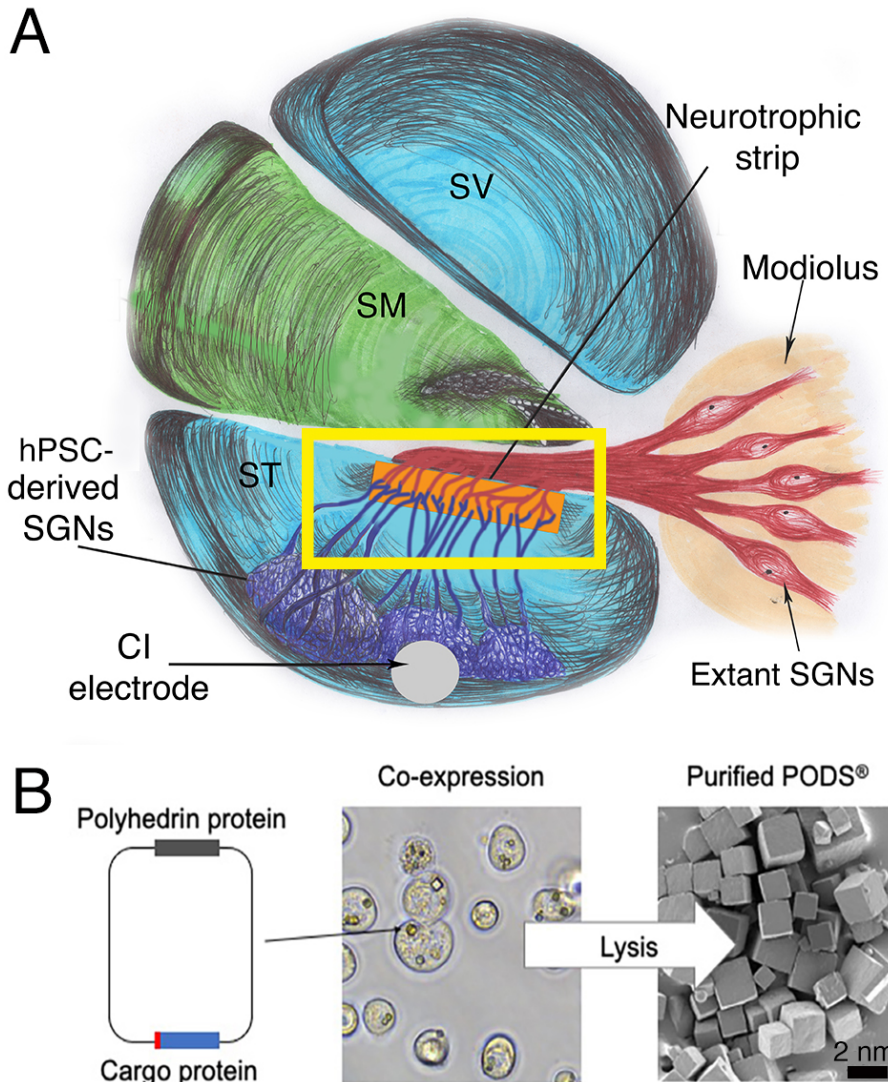


Figure 1: (A): A next-generation bioactive CI and a neurotrophic strip. The neural network in this scheme consists of a CI electrode, transplanted stem cell-derived SGNs, the neurotrophic strip, and extant/endogenous SGNs (red). Note that neuronal connection is largely absent with hair cells (not shown). (B): Polyhedrin Delivery System (PODS)®. PODS® crystals are cubic protein co-crystals produced by Sf9 cells (a clonal isolate of *Spodoptera frugiperda* Sf21 cells [IPLB-Sf21-AE], in which the polyhedrin protein and a second protein are co-expressed). This second protein is termed as the active, or cargo protein (Figure 1B, left). Inside the Sf9 cells, polyhedrin proteins self-assemble into cubic crystals (Figure 1B, center) while the active protein, tagged with a short peptide sequence, binds to the growing polyhedrin crystal. The crystals are extracted and purified by simple cell lysis and washes to remove cell debris (Scanning electron micrograph, Figure 1B, right).

62 that PODS<sup>®</sup>-human neurotrophin system could stably provide and maintain  
63 an adequate neurotrophin gradient to hPSC-derived ONPs, facilitating otic neu-  
64 ronal differentiation and directional neurite outgrowth. To test this hypothesis,  
65 we first devised a finite element model (FEM) to simulate the *in vitro* neu-  
66 rotrophin gradient generated by PODS<sup>®</sup>. In this study, we focus on the role of  
67 BDNF—the most studied of the neurotrophins in the inner ear, and the most  
68 vital for the functional recovery of damaged SGNs [20]. For biological validation  
69 and demonstration we used a multi-chamber microfluidic device, which mimics  
70 the *in vivo* micro-environment of the inner ear more so than conventional lab-  
71 oratory plates in terms of volume and concentrations of endogenous/exogenous  
72 factors [21].

73 **2. Materials and Methods**

74 *2.1. Polyhedrin delivery system*

75 The Polyhedrin Delivery System (PODS<sup>®</sup>-human BDNF [rhBDNF]) (Cell  
76 Guidance Systems, Cambridge, United Kingdom) was used as a self sustaining  
77 source of rhBDNF. PODS<sup>®</sup>-rhBDNF utilizes the polyhedrin protein formed  
78 by *Bombyx mori*, an insect from the moth family *Bombycidae*. A cargo pro-  
79 tein (i.e., rhBDNF) is co-expressed within the polyhedrin crystal and is slowly  
80 released with degradation of the PODS<sup>®</sup> crystals by cell-secreted proteases  
81 (Figure 1B)[9, 18, 22].

82 *2.2. Human pluripotent stem cell culture using dual-compartment microfluidic  
83 device*

84 Human embryonic stem cells (hESCs: H7 and H9, passages number 25–35)  
85 and were obtained from WiCell Research Institute (Madison, Wisconsin, USA).  
86 Human induced pluripotent stem cells (hiPSCs: TC-1133HKK, passage num-  
87 ber 22–35) were generated from human CD34+ cord blood cells using the four  
88 Yamanaka factors at Lonza (Walkersville, Maryland [MD], USA). The hiPSC  
89 cell line (TC-1133HKK) was kindly provided by Healios K.K. (Tokyo, Japan).

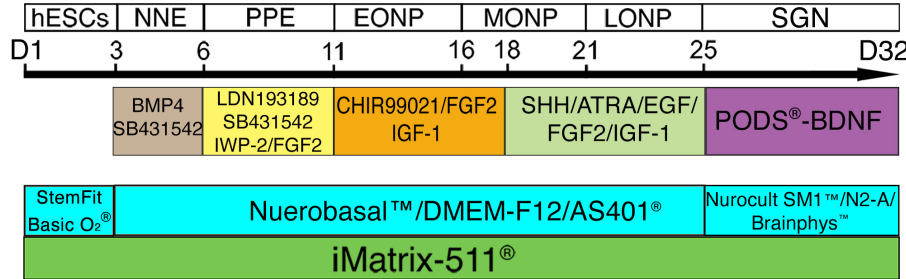


Figure 2: Overview of otic neuronal differentiation protocol for hPSCs. Please see detail in [8, 9, 23, 24] and the Supplemental Data. Each developmental stage is shown at the top, with key treatments shown below. NNE: nonneuronal ectoderm; PPE: preplacodal ectoderm; EONP: early-stage otic neuronal progenitor; MONP: mid-stage otic neuronal progenitor; LONP: late-stage otic neuronal progenitor; BMP4: bone morphogenetic protein 4; SHH: Sonic hedgehog; ATRA: all-trans retinoic acid; EGF: epidermal growth factor; IGF-1: insulin-like growth factor-1; FGF2: fibroblast growth factor 2; N2B27-CDM: chemically defined medium containing N2 and B27 supplements.

90 hPSC-derived ONPs were derived based on our previously established protocol  
 91 (Supplemental Data) [8, 9, 23, 24]. A step-wise series of ligands and growth  
 92 factors was added to a neuronal induction medium to promote hPSC differen-  
 93 tiation toward the late-stage ONP lineage—mitotic progenitor population that  
 94 generates the SGNs. (Figure 2).

95 Microfluidic devices provide a platform for specifically evaluating axonal re-  
 96 generation [25]. Here, multi-chamber microfluidic devices, Xona™ Microfluidics  
 97 XC150 and XC450 (Xona™ Microfluidics, Research Triangle Park, North Car-  
 98 olina, USA), were used for computational calculation and biological validation  
 99 (Figure 3A–B). The Xona™ device allows for neurites to grow toward growth  
 100 factors in the opposite chamber while limiting migration of derived ONP cell  
 101 bodies due to specific dimensions of the device. Additionally, the microchannel  
 102 array between the two chambers mimics the porous bony separation between  
 103 the modiolus (where extant SGNs are localized) and the scala tympani (where  
 104 the biohybrid CI will be implanted). Thus the diffusion profile of the released  
 105 rhBDNF *in vitro* more accurately predicts that of the *in vivo*.

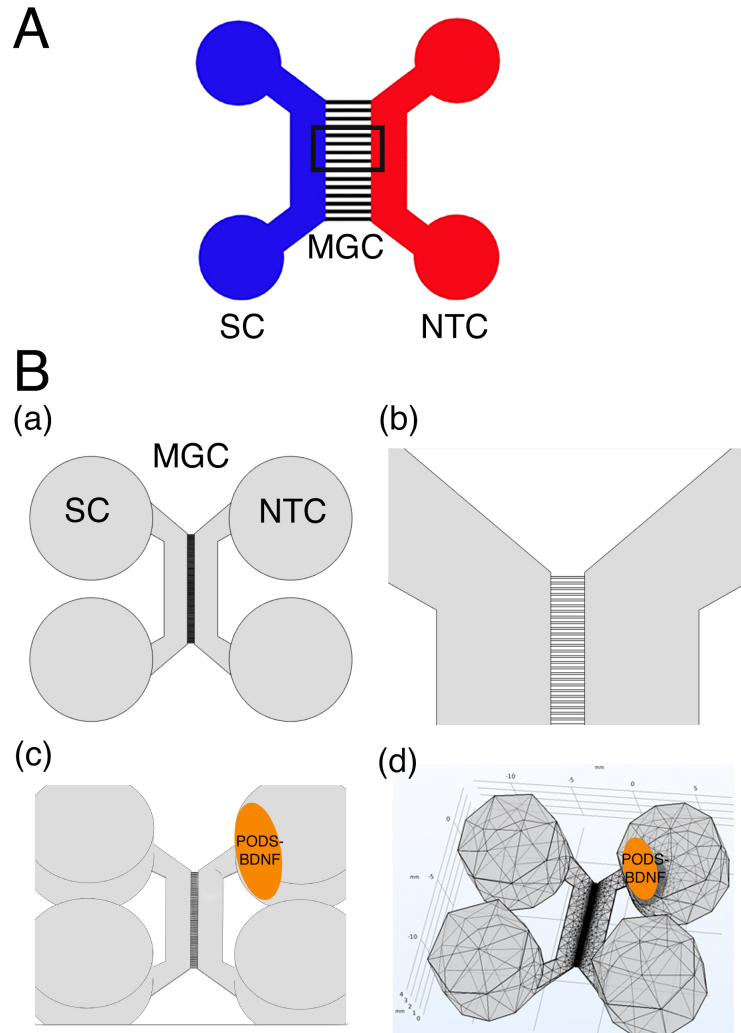


Figure 3: (A): Schematic specification of a Xona™ Microfluidics XC 450. Two main channels (somal compartment (SC) and neurotrophin compartment (NTC)) on either side are connected by a micro-groove channel (MGC) spanning  $450 \mu\text{m}$  with a width of  $10 \mu\text{m}$  (black square). The somal compartment contains hPSC-derived late-stage ONPs (shown in black), while the neurotrophin compartment contains the secreted factors (i.e., BDNF) that are released from PODS®-rhBDNF crystals. (B):(a) Xona™ Microfluidics XC450 device geometry, created at a 1:1 scale with Autodesk Inventor®, in which the diffusion profile of the released BDNF was modeled and tested. (b) Detail of the microchannels joining the two compartments of the Xona™ Microfluidics XC450. (c) Xona™ Microfluidics XC450 device showing the optimized area and geometry to localize PODS® containing rhBDNF (yellow ellipsoid area). (d): Mesh geometry of the Xona™ XC450 generated with Autodesk Inventor, depicting the localized volume of PODS®-rhBDNF ( $1 \mu\text{L}$ ) as an ellipsoid disk.

106 The devices were washed and coated with poly-L-ornithine (PLO, 20  $\mu$ g/mL  
107 in H<sub>2</sub>O, Sigma-Aldrich, St. Louis, Missouri [MO], USA) and recombinant  
108 laminin-511 (iMatrix-511, 0.5 mg/mL, Nacalai USA, San Diego, California [CA],  
109 USA) according to the manufacturer-outlined protocol. Next, approximately  
110 1.75 x 10<sup>5</sup> cells (in 20  $\mu$ L of media) were added through the top and bottom left  
111 wells to the somal compartment (i.e., the total amount of 3.5 x 10<sup>5</sup> hPSC-derived  
112 ONPs were added).

113 PODS®-rhBDNF were placed in the top right well of the neurotrophin com-  
114 partment (Figure 3A–B) to generate a BDNF concentration gradient to promote  
115 directional neurite growth. hPSC-derived ONPs were cultured for 7 days in the  
116 Xona™ device to induce otic neuronal differentiation. Note that due to our  
117 use of the microfluidic device, high-density cell cultures were induced to facili-  
118 tate molecular studies as well as the generation of a more biologically relevant  
119 neuronal phenotype (i.e., otic lineage) [25]. Media was topped off daily after  
120 imaging (from 20–40  $\mu$ L per well).

121 *2.3. Enzyme-linked immunosorbent assay for brain-derived neurotrophic factor*

122 In order to determine the release and degradation kinetics of PODS®-  
123 rhBDNF, an experiment measuring concentrations at sequential time points was  
124 performed. To measure the concentration of rhBDNF secreted from PODS®-  
125 rhBDNF crystals, the culture media from both a control and an experimental  
126 condition were collected at each time point and immediately stored at -80°C  
127 before running an enzyme-linked immunosorbent assay (ELISA) after the final  
128 collection. The same method was applied to measure the degradation kinet-  
129 ics of rhBDNF protein with a carrier protein (Bovine Serum Albumin [BSA])  
130 (#248-BDB-050, R&D Systems, Minneapolis, Minnesota, USA). Experimen-  
131 tal conditions were culture media enriched with 10% fetal bovine serum (FBS)  
132 (Thermo Fisher Scientific, Waltham, MA, USA). All samples were quantified  
133 with a BDNF ELISA kit (# BGK23560; PeproTech, Rocky Hill, New Jersey,  
134 USA), and the results were analyzed with a Synergy HTX Multi-Mode Reader  
135 (BioTek, Winocski, Vermont, USA) at a 450 nm wavelength, as instructed by

136 the manufacturer. Release and degradation kinetics were then calculated using  
137 MATLAB Curve Fitting Toolbox (MathWorks, Natick, CA, USA).

138 *2.4. Sodium dodecyl sulphate-polyacrylamide gel electrophoresis*

139 Sodium dodecyl-sulfate polyacrylamide gel electrophoresis (SDS-PAGE) is  
140 commonly used as a method to separate proteins with molecular masses be-  
141 tween 5 and 250 kDa [26], a range of which is suitable for detecting human  
142 BDNF protein (molecular weight [MW]: 14kDa [27]) and polyhedrin (MW: ~29  
143 kDa [22]). In this study, SDS-PAGE was used to assess the molar ratio of  
144 BDNF to polyhedrin in each sample. Briefly, each protein sample was diluted  
145 in deionized water and mixed with 6x Laemmli sample buffer (Bio-Rad Labora-  
146 tories, Inc., Des Plaines, Illinois [IL], USA) containing 2-mercaptoethanol and  
147 heated at 100°C for 5 to 20 minutes. Samples were then loaded into precast  
148 Mini-PROTEAN TGX 4-15% polyacrylamide mini-gels (Bio-Rad Laboratories,  
149 Inc., Des Plaines, IL, USA). Then, 5 mL of Precision Plus Protein Kaleido-  
150 scope Prestained Protein Standards (Bio-Rad Laboratories, Inc., Des Plaines,  
151 IL, USA) were loaded in each gel run. Electrophoresis was performed at room  
152 temperature for approximately 90 minutes using a constant voltage (100V) in  
153 1x solution of Tris-Glycine-SDS electrophoresis buffer (Bio-Rad Laboratories,  
154 Inc., Des Plaines, IL, USA) until the dye front reached the end of the 60 mm  
155 gel. After electrophoresis, the mini-gels were rinsed with deionized water 3  
156 times for 5 minutes and were subsequently incubated in SimplyBlue™ SafeStain  
157 (ThermoFisher Scientific, Waltham, MA, USA) for one hour at room temper-  
158 ature with gently agitation. Images obtained from gels were analyzed using  
159 ImageJ 1.53g (December 4, 2020, the National Institutes of Health, Bethesda,  
160 MD, USA [28]). The calculated molar ratio was applied to the COMSOL®  
161 Multiphysics model to accurately predict the amount of rhBDNF released from  
162 PODS®-rhBDNF. SDS-PAGE was performed according to the manufacturer's  
163 technical guide (Bio-Rad Laboratories, Inc., Des Plaines, IL, USA).

164     *2.5. Western Blot*

165     The identity of the BDNF protein detected by SDS PAGE was verified by  
166     western blot (Bio-Rad Laboratories, Inc., Des Plaines, IL, USA). Briefly, the  
167     polyvinylidene difluoride (PVDF) membrane was prepared in methanol for 30  
168     seconds before soaking in 1x Tris-Glycine-Methanol transfer buffer for 10 min-  
169     utes. Wet transfer was performed at 4°C for approximately 60 minutes using a  
170     constant voltage (100V) in 1X solution of Tris-Glycine-Methanol transfer buffer.  
171     After transfer, the membrane was briefly rinsed with 1X Tris-buffered saline  
172     Tween-20 (TBST) and was subsequently blocked in 5% BSA in TBST for 24  
173     hours at 4°C with gentle agitation. The membrane was then rinsed with 1x  
174     TBST before incubating in BDNF polyclonal antibody (ThermoFisher Scien-  
175     tific, Waltham, MA, USA) diluted to 1:1500 in 1% BSA in TBST for 24 hours at  
176     4°C with gentle agitation. Following incubation, the membrane was rinsed in 1x  
177     TBST 5 times for 5 minutes to remove unbound primary antibody. Then, the  
178     membrane was incubated in Goat anti-Rabbit IgG (H+L) horseradish peroxy-  
179     dase (HRP) conjugated secondary antibody (ThermoFisher Scientific, Waltham,  
180     MA, USA) diluted to 1:5000 in 1% BSA in TBST for one hour at room tem-  
181     perature with gentle agitation. Following incubation, the membrane was rinsed  
182     in 1x TBST 5 times for 5 minutes to remove unbound secondary antibody. For  
183     sensitive detection, the membrane was treated with Pierce™ ECL Western Blot-  
184     ting Substrate (ThermoFisher Scientific, Waltham, MA, USA), and visualized  
185     using an Azure 600 Digital Imager (Azure Biosystems, Dublin, CA, USA). Elec-  
186     trophoresis buffer for sample condition and run condition was summarized in  
187     Supplementary Table S1.

188     *2.6. Three-dimensional finite element model*

189     We used finite element analysis (FEA) to simulate the BDNF concentration  
190     gradient in a multi-chamber microfluidic device during release and subsequent  
191     degradation. FEA is a computational numerical technique, which approximates  
192     mathematical solutions to partial differential equations (PDEs) that appropri-  
193     ately simulate complex real-world problems. In this study, the finite element

model allowed us to predict the concentration gradient with respect to time in the multi-chamber microfluidic device, depending on the number of PODS®-rhBDNF introduced into the system. To solve the finite element model, we used COMSOL® Multiphysics (version 5.6 [released on November 11, 2020], COMSOL, Inc., Burlington, Massachusetts [MA], USA), which is a finite element method solution tool for engineering and scientific research computations. We used sustained-release kinetics for PODS®-rhBDNF determined from an ELISA study (see next subsection) as well as data from a previous study from our group [9]. Device geometry was generated at a 1:1 scale using Autodesk® Inventor 2019.0.2 (Autodesk, Mill Valley, CA, USA) (Figure 3B). The computational analysis was implemented on a high-performance desktop computer platform equipped with a CPU (AMD Ryzen Threadripper 3990X 64-Core, 128-Thread @ 4.3 GHz) with 64 GB RAM, and two GPU cards (NVIDIA GeForce RTX 3080Ti, 12GB 384-bit GFF6X Graphics card).

### 2.7. Immunocytochemistry and image acquisition

Glass coverslips (Corning Inc., Corning, New York, USA) were coated with poly-d-lysine (PDL) (#A3890401, ThermoFisher Scientific, Waltham, MA, USA) and poly-ornithine (PLO) (# A-004-C, MilliporeSigma, St. Louis, MO, USA) affixed to a somal compartment as per the manufacturer's instructions. A total of 100,000 dissociated hPSC-derived ONPs were plated onto a somal compartment of the device. On Day 7, 4% (w/v) paraformaldehyde (PFA) (ThermoFisher Scientific, Waltham, MA, USA) was added to the compartments for 20 minutes to fix the cells. ICC was used to stain for GATA3, PAX8, and beta-III tubulin. These three proteins have shown to appropriately characterize ONPs in our previous studies [8, 9, 24]. Following PBS wash, cultures were blocked with 5% BSA at room temperature for 1 hour. Cultures were then incubated overnight at 4°C on a shaker plate in primary antibody solution using Rabbit anti-Beta-III-Tubulin (1:100, Abcam, Cambridge, MA, USA), Goat anti-PAX8 (1:500, Abcam, Cambridge, MA, USA), and Mouse anti-GATA3 (1:500, R&D Systems, Minneapolis, MN, USA). Following PBS washes, cultures

were incubated at room temperature for 90 minutes on a shaker plate in secondary antibody solution composed of Alexafluor647 anti-Rabbit (1:1000, ThermoFisher Scientific, St. Louis, MO, USA), Alexafluor488 anti-Goat (1:1000, ThermoFisher Scientific, St. Louis, MO, USA), and Alexafluor594 anti-Mouse (1:1000, ThermoFisher Scientific, St. Louis, MO, USA) in 1% BSA. Following PBS -/- washes, cultures were incubated with DAPI for 20 minutes (300 nM, ThermoFisher Scientific, St. Louis, MO, USA). Secondary antibody controls were performed each time multiple primary antibodies were used [29]. Labeling controls (detection controls) were performed for a sample from each batch of hPSC culture [29]. See Supplementary Figure S1 for exemplary figures for these control conditions. Results were imaged using a Nikon Ti2 Widefield Laser Microscope System (Nikon, Tokyo, Japan). Phase-contrast images were captured on a Nikon Eclipse TE2000-U inverted microscope (Nikon, Tokyo, Japan). All fluorescence images were acquired on a Zeiss LSM 510 META laser-scanning confocal microscope (Carl Zeiss, Oberkochen, Germany), a Nikon Ti2 laser laser-scanning confocal microscope (Nikon, Tokyo, Japan), or a Leica SP5 laser-scanning confocal microscope (Leica, Welzlar, Germany). Observers were blinded to the conditions during imaging and tracing. In general, the images were processed with a Image J ver. 1.53j or Matlab R2020b. Further detail on image acquisition and quantification of fluorescent-positive cells can be found in the Supplemental Data.

#### *2.8. Preferred cell orientation analysis*

Collective cell migration, where cells organized in a tightly connected fashion migrate as cohesive structures, is a critical biological process to highlight the neurotrophin diffusion gradient profile [30]. To evaluate this process, time-lapse acquisition of images of the Xona™ device was performed using an inverted microscope (Nikon Eclipse TS100, Tokyo, Japan) at Day 1, 3, 5, and 7. Due to the high cell density required for hPSC-ONPs to survive in the somal compartment of the Xona™ device, images were not amenable to manual analysis in most of the cases. To circumvent this problem, we performed a series of image pre-

254 processings that are mainly based on modified binarization-based extraction of  
255 aliment score methods with some modifications [31]. We used MATLAB Im-  
256 age Processing Toolbox R2020b (version 9.9.0.1495850, September 30th, 2020,  
257 Mathworks, Natick, MA) for analysis. Please see Supplementary Figure S2 for  
258 further detail. The analysis of directional data in general represents a particu-  
259 lar challenge: there is no reason to designate any particular point on the circle  
260 as zero, as it is somewhat arbitrary depending on where one sets a coordinate  
261 [32, 33]. In this study, we used polar coordinates to determine the directionality  
262 of preferred cell orientation. For this analysis, we again used MATLAB Image  
263 Processing Toolbox R2020b. See detailed discussion on how we determined the  
264 preferred cell orientation in Supplementary Figure S3.

265 *2.9. Neurite alignment vector assay, neurite growth assay and cell migration*  
266 *assay*

267 The microfluidic device allowed us to culture hPSC-derived ONPs in a po-  
268 larized manner and to directly isolate/analyze neurites. To evaluate the neurite  
269 projection into the neurotrophin compartment by derived otic neurons cultured  
270 in the somal compartment, we performed a neurite alignment vector assay. We  
271 also evaluated the length of neurites that grew from hPSC-derived ONPs. For  
272 these purposes, hPSC-derived ONPs were cultured in a Xona™ XC450 for seven  
273 days and then immunostained with *beta*-III tubulin and DAPI. We used two  
274 ImageJ plug-in toolkits, NeuriteTracer and NeuronJ, to assess neurite align-  
275 ment and neurite growth [34, 35]. Due to the bipolar nature of hPSC-derived  
276 ONPs/SGNs, we measured the two longest neurites from the cells [24, 36].  
277 Please see Supplementary Figure S4 for detailed description of this analysis. We  
278 used hPSC-derived ONPs cultured with 800,000 PODS®-rhBDNF as a positive  
279 control. The number 800,000 was chosen based on our FEM in that there was  
280 no neurotrophin gradient in a somal compartment. As a negative control, we  
281 used 20 ng/mL of recombinant human BDNF. To evaluate cell migration across  
282 a microgroove channel, we performed cell migration analysis. We manually  
283 counted the number of ONPs that migrated from the somal compartment into

284 the microchannels, as well as the neurotrophin compartment.

285 *2.10. Statistical analysis*

286 When appropriate, and as indicated in each figure, statistical analysis was  
287 performed. Experimental values are typically expressed as mean and standard  
288 error (SE). The majority of the statistical analyses were performed with Python  
289 3.9.6. (Python Software Foundation, Wilmington, Delaware, USA). The follow-  
290 ing libraries were used for the statistical analysis: Scipy, Numpy, Matplotlib,  
291 and Seaborn [37, 38, 39]. Normal distributions were assumed unless mentioned  
292 otherwise.  $P$  values smaller than 0.05 were considered statistically significant.  
293 For circular statistics, we derived the sample mean vector and its polar coor-  
294 dinate. Mean and confidence intervals were calculated. We chose confidence  
295 coefficient,  $Q$ , e.g.  $Q = 0.95$ . To analyze the axial nature of data, especially to  
296 compute the mean vector angle, we doubled each angle and reduced the mul-  
297 tiples modulo  $360^\circ$ . Please see detailed discussion in Supplementary Figure S3  
298 and S5. The Rayleigh test of uniformity and V-test were performed to deter-  
299 mine whether the samples differ significantly from randomness (i.e., where there  
300 is statistical evidence of directionality). One-sample test for the mean angle was  
301 performed to test whether the population mean angle is statistically different  
302 from the given angle. In all of our circular statistics, von Mises distribution was  
303 assumed and also verified. Circular statistics were performed using CircStat: A  
304 MATLAB Toolbox [33, 40]. Please see detailed description of circular statistics  
305 in Supplementary Figure S3 and S5. Experiments were done in three biological  
306 replicates unless otherwise specified in Figure captions.

307 **3. Results**

The appropriate number of PODS®-rhBDNF crystals to induce an effective neurotrophin gradient for otic neuronal differentiation and directed neurite outgrowth was calculated using a three-dimensional FEA that predicts the concentration profile of BDNF formed through the gradual release and diffusion

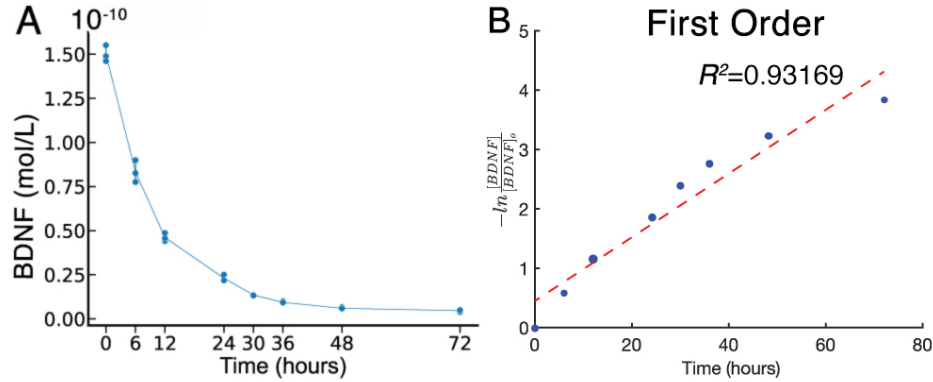


Figure 4: Chemical kinetics of Brain Derived Neurotrophic Factor (BDNF). (A): Concentration of rhBDNF in solution over 72 hours after initial application. (B):  $\frac{1}{[BDNF]}$  data fit to first order curve. Please see other curve fit data in Supplemental Figure 1. Red line: fitted line, blue dots: individual data point.  $k_2$  is defined as slope of fitted curve.

of BDNF from PODS<sup>®</sup>-rhBDNF. First, we quantified the chemical kinetics of this phenomenon with ELISA testing (Figure 4) to establish the parameters for the FEA. Here, two consecutive chemical reactions occur: 1) the breakdown of PODS<sup>®</sup> crystals into polyhedrin protein and rhBDNF, and 2) the degradation of rhBDNF toward the degradation product (Equation (1)). Equation (1) omits the reaction product polyhedrin due to its irrelevance in the next reaction.



where  $DP$  is the degradation product of the released rhBDNF, and  $k_1$  and  $k_2$  are the rate constants ( $\frac{1}{hour}$ ) for their respective reactions.

Degradation kinetics data for rhBDNF was collected while monitoring rhBDNF concentration after introducing a predefined amount into a single well of solution. The data obtained throughout the first 72 hours indicate an exponential decay, suggesting first order kinetics (Figure 4). To confirm this notion, we performed a linear and nonlinear least square analysis of the kinetic data with the MATLAB Curve Fitting Toolbox. We found that the corresponding  $R^2$  was 0.93169 for the first order curve-fit, confirming that the degradation kinetics

317 was indeed first order. The value for  $k_2$  ( $0.0679 (\frac{1}{hour})$ ) was derived from  
 318 the curve-fit (See further detail in Supplementary Figure S7). Furthermore,  
 319 data for the complete chemical reaction were collected by monitoring rhBDNF  
 320 concentration over time after placing a predefined amount of PODS<sup>®</sup>-rhBDNF  
 321 into a single well of solution. The data collected appeared to fit the curve for  
 322 Equation 2, which describes the concentration of the intermediate product of  
 323 two consecutive first order reactions:

$$C_{rhBDNF} = C_{PODS} \cdot k_1 \cdot \left( \frac{e^{-k_1 \cdot t}}{k_2 - k_1} + \frac{e^{-k_2 \cdot t}}{k_1 - k_2} \right) \quad (2)$$

324 where  $C_{rhBDNF}$  is the concentration of rhBDNF and  $C_{PODS}$  is the concentra-  
 325 tion of PODS<sup>®</sup> [43].

326 We successfully fit the data to this equation's respective curve and empir-  
 327 ically approximated  $k_1$  to be  $0.00686 (\frac{1}{hour})$  after plugging in our value for  $k_2$   
 328 (See further detail in Supplementary Figure S7). Using these calculated rate  
 329 constants, the resulting chemical gradient over time after PODS<sup>®</sup>-rhBDNF  
 330 placement can be solved for any geometry by applying Fick's second Law of  
 331 diffusion (Equation 3) and the appropriate boundary (Equations 4 and 5) and  
 332 initial conditions (Equation 6):

$$\frac{dC}{dt} = \nabla \cdot (\nabla C \cdot D) - k_2 \cdot C \quad (3)$$

Boundary conditions:

$$\delta C \Big|_{walls} = 0 \quad (4)$$

333 and

$$\delta C \Big|_{PODS} = k_1 \cdot PODS_0 \cdot e^{-k_1 \cdot t} \quad (5)$$

Initial conditions:

$$C \Big|_{t=0} = 0 \quad (6)$$

334 where  $C$  is the concentration of rhBDNF,  $D$  is diffusivity of rhBDNF (6.76  
335  $\frac{mm^2}{day}$  [44]),  $-k_2 \cdot C$  is the sink term corresponding to the degradation and cell-  
336 utilization of the rhBDNF, and  $PODS_0$  is the initial concentration of the cargo  
337 protein (i.e., BDNF) within the PODS® crystals. The first boundary condition  
338 (Equation 4) shows that the concentrations of rhBDNF at the walls of the  
339 microfluidic device are fixed at 0. The second boundary condition (Equation 5)  
340 represents the exponential nature of the decay of PODS®. Note that both are  
341 Neumann boundary conditions.

342 We first empirically tested two available microchannel lengths—(i.e., Xona™ -  
343 XC150 [ $150\text{ }\mu\text{m}$ ] and Xona™ -XC450 [ $450\text{ }\mu\text{m}$ ]). This was done initially because  
344 mass (i.e., BDNF) transport from the neurotrophin compartment through the  
345 micro-groove channels into the somal compartment is an important factor in  
346 generating the concentration gradient *via* diffusion mixing. We determined that  
347 the Xona™ Microfluidics XC450 was more appropriate for this study as the XC-  
348 150's micro-groove channels were not long enough to generate the appropriate  
349 concentration gradient throughout the somal compartment. This feature is rel-  
350 evant to human inner ear because the micro-groove channels in the Xona device  
351 simulates the presence of the osseous spiral lamina and modiolus between the  
352 scala tympani and SGNs [41, 42]. Following device selection, we generated a  
353 three-dimensional geometry mesh of the Xona™ Microfluidics XC450 for the  
354 FEA (Figure 3B(d)). Please also see Supplementary Figure S6 for detailed  
355 measurements of the mesh.

356 As mentioned, we used the first-order fitted data from our ELISA experi-  
357 ment and then determined the values of the  $k_{1,2}$  coefficients, which were then  
358 applied to the diffusion equation. The finite element model was then computed  
359 for different PODS®-rhBDNF concentrations and time intervals to optimize  
360 the rhBDNF concentration gradient for hPSC-derived ONP differentiation into  
361 SGNs as well as directed neurite extension. Figure 5 shows FEM-computed  
362 rhBDNF concentration gradients for 20,000 PODS®-rhBDNF from Day 1–7.  
363 Note that the rhBDNF concentrations were greater on D2–5 to promote neu-  
364 ronal differentiation and neurite outgrowth observed on D7 (Figure 5B). Com-

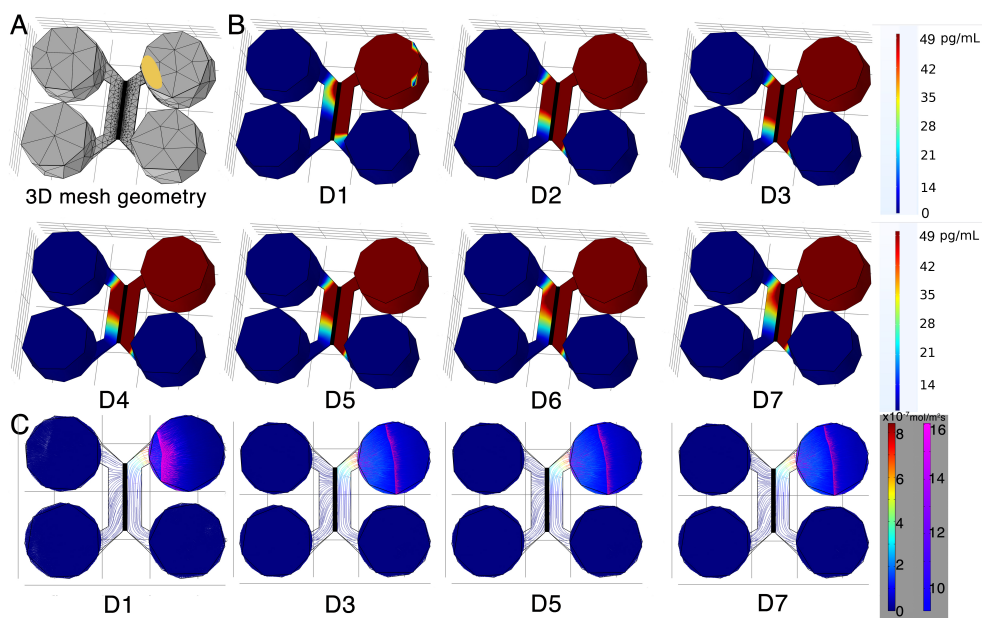


Figure 5: (A): 3D mesh geometry of a Xona™ XC450 created with Autodesk Inventor. An ellipse-shaped PODS®-rhBDNF disc is shown in yellow. (B): rhBDNF concentration gradient for 20,000 PODS®-rhBDNF from D1–D7. Note that the model does not account for media changes during the culture period. The corresponding color map shown has a range from 0 ng/mL to 49 pg/mL. (C): Diffusion flux ( $mol/m^2s$ ) was computed using COMSOL Chemical Engineering module on D1, D3, D5, and D7.

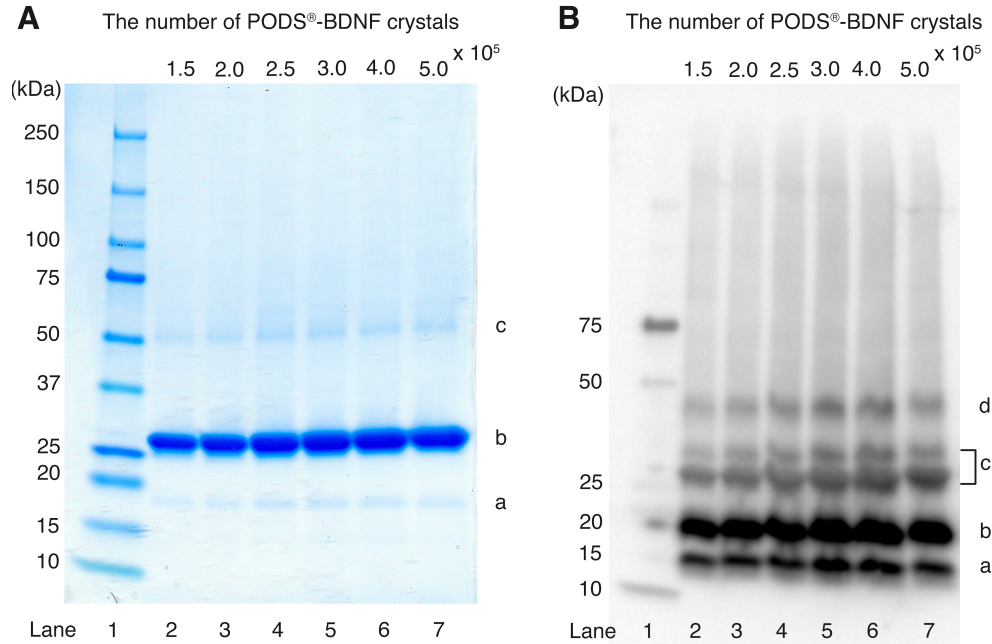


Figure 6: (A): SDS-PAGE analysis of PODS<sup>®</sup>-rhBDNF. Samples containing six quantities of PODS<sup>®</sup>-rhBDNF crystals were run on precast 4-15% polyacrylamide mini-gels and stained with Coomassie G-250 solution for visualization. Protein bands appear at approximately 18.8 (a), 28.0 (b), and 46.8 kDa (c). Lane 1: molecular weight marker. Lanes 2-7: samples containing

365 puted diffusion flux was uniform throughout D1–7 (Figure 5C). Also note that  
 366 highest concentration of rhBDNF released from PODS<sup>®</sup>-crystals was greater  
 367 than 50 pg/mL, the concentration sufficient for otic neuronal differentiation  
 368 and neurite outgrowth of hPSC-derived ONP 3D spheroids from our previously  
 369 published data [9]. Optimization of the adequate number of PODS<sup>®</sup>-rhBDNF  
 370 was performed empirically; we also performed FEA with 10,000 and 40,000  
 371 PODS<sup>®</sup>-rhBDNF. Please see detailed discussion for the empirical optimization  
 372 in Supplementary Figure S8.

373 SDS-PAGE was used to separate PODS<sup>®</sup>-rhBDNF crystals into its con-  
 374 stituent proteins to determine the molar ratio of polyhedrin to rhBDNF. Vi-  
 375 sualization with Coomassie G-250 solution (Figure 6A) revealed three distinct

376 protein bands at 18.8 (a), 28.0 (b), and 46.8 (c) kDa, which correspond with  
377 the molecular weights of H1-tagged BDNF monomer, polyhedrin, and H1-tagged  
378 BDNF monomer attached with polyhedrin, respectively. Western blot analy-  
379 sis was subsequently conducted to confirm the identity of the 18.8 kDa band  
380 as rhBDNF. Enhanced chemiluminescence (Figure 6B) revealed four protein  
381 bands at 14.0 (a), 18.8 (b), 37.6 (c), and 46.8 (d) kDa, which correspond with  
382 the molecular weights of rhBDNF monomer, H1-tagged BDNF monomer, H1-  
383 tagged BDNF dimer, and H1-tagged BDNF monomer attached with polyhedrin.  
384 Immunoblot detection of the 18.8 kDa band further implicates its identity as  
385 rhBDNF. SDS-PAGE images were converted to 8-bit grayscale and mean cor-  
386 rected integrated pixel intensity values were calculated for protein bands located  
387 at 28.0 and 18.8 kDa; the protein band detected at 46.8 kDa was omitted from  
388 the final computation based on the notion that it contained a 1:1 ratio of poly-  
389 hedrin to BDNF. Results indicate that the molecular ratio of polyhedrin to  
390 rhBDNF is approximately 17:1.

391 To objectively compare the degree of otic neuronal differentiation in hPSC-  
392 derived ONPs, we performed quantitative analysis of PAX8 and GATA3 double-  
393 positive cells using immunocytochemistry. We chose PAX8 and GATA3 for this  
394 analysis because our previous studies indicated high expression of these protein  
395 markers in late-stage ONPs and early-stage SGNs [8, 9, 24]. Cells were stained in  
396 the somal compartment of the Xona™ device, highlighted in green in Figure 7A.  
397 Figure 7B shows the resulting image of cells in the somal compartment, and  
398 a heat-map representation of the percentage of double-positive cells is shown  
399 in Figure 7C. It should be noted here that the heatmap is sensitive to the  
400 differences in cell density across channel. This was accounted by averaging  
401 the double-positivity across three biological replicates. The heat-map indicates  
402 higher double-positivity in the upper region of the somal compartment, which  
403 is closest to the PODS®-rhBDNF disc placement (shown in a orange ellipse in  
404 Figure 7A) in the neurotrophin compartment. Double-positivity decreases in  
405 the somal compartment as distance from the PODS®-rhBDNF disk increases,  
406 supporting the presence of a BDNF neurotrophin gradient as predicted by our

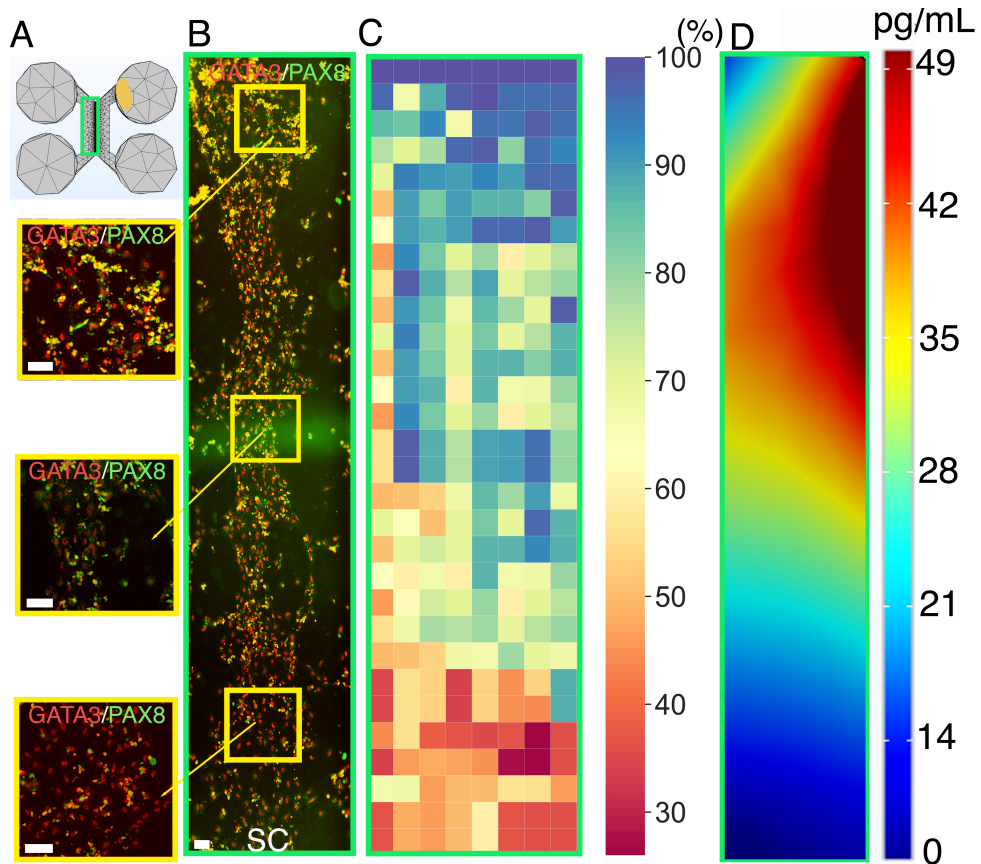


Figure 7: Human PSC-derived late-stage ONPs grown in a microfluidic device at Day 7 were stained for GATA3 (red) and PAX8 (green). (A): Geometry mesh of the microfluidic device Xona™ XC450 generated by Autodesk Inventor. The green square indicates the cell seeding location in the somal compartment of the device. An ellipse-shaped PODS®-rhBDNF disc is shown in yellow. (B): Cells were analyzed by staining with neuronal markers GATA3 (red) and PAX8 (green). Yellow highlighted regions are magnified on the left. SC: somal compartment. (C): Heat-map representation of double-positivity of hPSC-derived ONPs in the device for GATA3 and PAX8 ( $n = 3$ ). Double-positivity increases from the lower to the upper portion of the somal compartment, suggesting that the higher BDNF concentration in the upper portion of the device improves differentiation. Scale bar: 100  $\mu\text{m}$ . (D): Prediction of BDNF concentration gradient released from PODS®-rhBDNF at seven days in culture using a finite element model. The corresponding color map is shown with a range from 0–49 pg/mL.

407 computational model calculation (Figure 7D).

408 We defined two hypothetical directional angles to predict the orientation of  
409 hPSC-derived ONPs and neurite growth (Figure 8). The  $n$ -dimensional Eu-  
410 clidean space, denoted by  $\mathbb{R}^n$ , is a linear vector space in that we can use polar  
411 coordinates to compute the directionality of cells and neurites [45]. Here, we  
412 used  $n = 1$  and 2. For one-dimensional Euclidean space ( $n = 1$ ), we simply drew  
413 a line for the Euclidean distance—the shortest distance between two points as  
414 shown in Figure 8A(b) (dark green lines). The two points were 1) the center  
415 point of a PODS®-rhBDNF disk ( $P$ ) and 2) the mid point of the medial side  
416 ( $Q_{1-5}$ ) (i.e., the near side to microgroove channels) of a pre-designated square  
417 (shown as a black square, zone 1–5 in Figure 8), respectively. The Euclidean  
418 distance angle (EDA),  $\phi_i$ , was defined as the angle between the horizontal line  
419 zero direction and the line  $PQ_i$  that consists of the Euclidean distance where  $i$   
420 = 1–5.

421 For two-dimensional Euclidean space ( $n = 2$ ), we utilized Fick's first law,  
422 which dictates that the diffusion flux ( $D$ ) is proportional to the concentration  
423 gradient ( $C$ ) [46]. Based on this theorem, the direction of a flow vector can  
424 be used to represent concentration gradient for the directionality. We hypothe-  
425 sized here that cell orientation is directionally controlled by the flux vector  
426 which is driven by the concentration gradient. Figure 8B shows the flow vectors  
427 in a somal compartment at Day 7 computed by COMSOL Chemical engineering  
428 module. We averaged the 10 flow vectors in each of five zones in Figure 8 to  
429 compute diffusion flux angle (DFA),  $\psi_i$ , where  $i = 1–5$  in Figure 8. To lighten  
430 the computational intensity, we reduced a dimension from 3D to 2D to com-  
431 pute diffusion Flux. Please see justification in Supplementary Data. All of the  
432 computed EDAs and DFAs can be found in Supplementary Table 2.

433 Figure 9 shows time-series of microscopic phase-contrast photomicrographs  
434 obtained on Day 1, 3, and 7 in the five zones in a Xona™ XC450. Each preferred  
435 orientation of any given cell was computed and then plotted on a polar diagram  
436 (blue circle). Mean vector angle (MVA, shown in red line on Figure 9) and  
437 median vector angle were computed. All of the polar diagrams in Figure 9 show

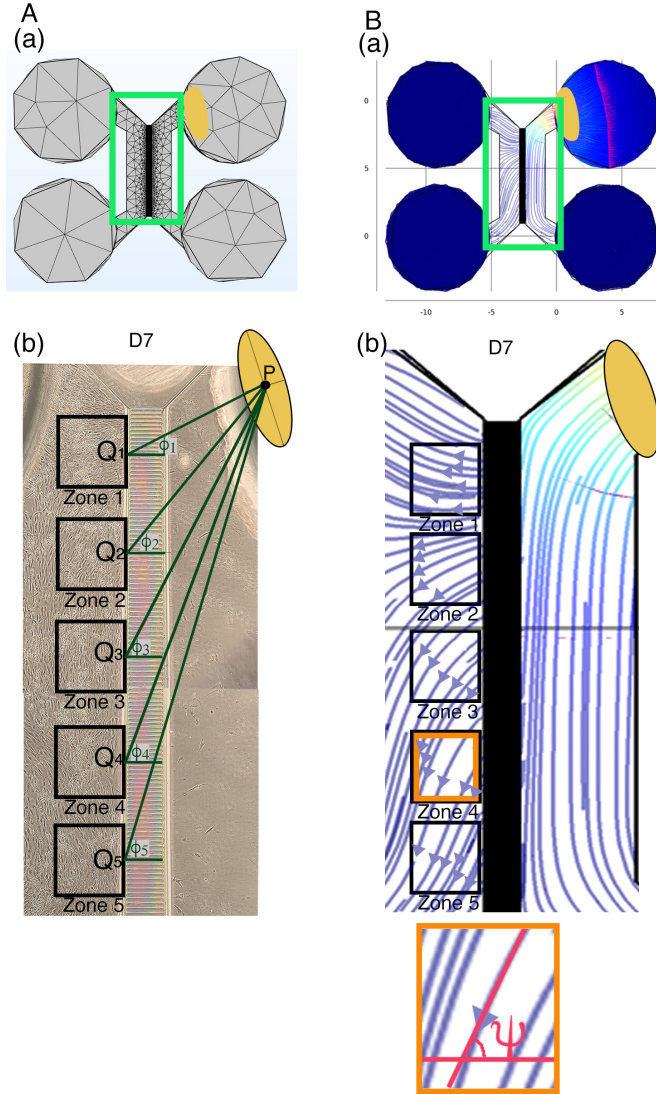


Figure 8: (A): Defining the Euclidean distance angle (EDA). (a) X-Y plane geometry mesh of a Xona™ XC450 device. Green square shows an area corresponding to a phase-contrast image below. An ellipse-shaped PODS®-rhBDNF disc is shown in yellow. (b) hPSC-derived ONPs were cultured in a Xona™ XC450 for seven days (D7). Yellow ellipse once again indicates the location of a disk contains PODS®-rhBDNF crystals (P: the center of this ellipse). In the somal compartment of the Xona™ XC450 device, we defined Zone 1–5, shown in black square. A line was drawn from the center of the PODS®-rhBDNF disk (P) to (Q<sub>1–5</sub>) (i.e., the near side to microgroove channels) of a pre-designated square (shown as a black square, zone 1–5) [i.e.,zone 1–5]. The Euclidean distance angle (EDA) for zone 1–5 was defined as  $\phi_i$ ,  $i = 1–5$ . (B): Defining diffusion flux angle (DFA). (a) Diffusion flux in a Xona™ XC450. Green squared area show a somal and neurotrophin compartment, which are magnified in (b). (b) Magnified image of diffusion flux of Zone 1–5 in a Xona™ XC450. Orange highlighted zone (zone 4) was magnified at the bottom of (b), defining a DFA ( $\psi$ ).

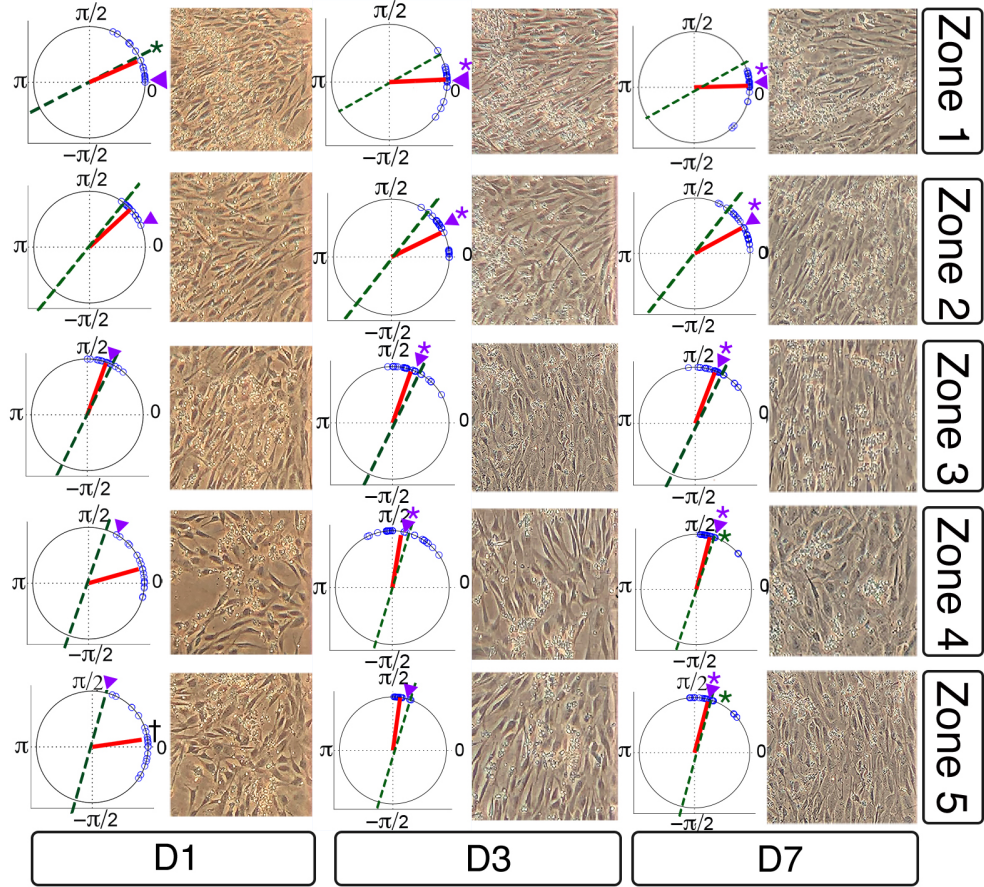


Figure 9: Preferred cell orientation analysis. Sequential phase-contrast images of a somal compartment of a Xona™ XC450 device in zone 1–5 (see Figure 8) on day 1 (D1), day 3 (D3), and day 7 (D7). A corresponding polar histogram indicates preferred orientation of hPSC-derived ONPs in an angle ( $0$ – $2\pi$  radians) in blue circles. Mean vector angle is shown in red line. Green dotted line shows Euclidean Distance Angle (EDA) and purple triangle indicates Diffusion Flow Angle (DFA). † symbol indicates that  $p$  value  $> 0.01$ . \* symbol indicates that the mean vector angle fits within the 95% confidence internal ( $\alpha < 0.05$ .)

438 that preferred orientation of hPSC-derived ONPs distribute in an unimodal dis-  
439 tribution. We also confirmed that a von Mises distribution is appropriate for  
440 these sets of data (See Supplementary Figure S9). We, therefore, then tested  
441 further to see if the cells had tendency to be oriented to a certain direction.  
442 To test this hypothesis, we used the Rayleigh test of uniformity to evaluate  
443 whether there is statistical evidence of circular directionality [32]. Computed  
444 *p* values for all the 15 conditions were less than 0.05, demonstrating that all  
445 of the conditions had statistically significant directionality. To further validate  
446 whether the observed angles have a tendency to cluster around the two hypo-  
447 thetical angles (i.e., EDA and DFA), we then performed the V test. Once again,  
448 *p* values for all 15 conditions were less than 0.05 except one (Zone 5 on Day 1),  
449 re-demonstrating that most of the conditions had statistically significant ten-  
450 dencies to cluster around the EDAs and DFAs. Finally, to investigate whether  
451 the preferred orientation of the cells were clustered around the EDAs or DFAs,  
452 we performed one sample test for the mean vector angle, which is similar to a  
453 one sample t-test on a linear scale. There was only one condition (Zone 1, day  
454 1) that was statistically significant for EDA, whereas most of the conditions on  
455 Day 3 and 7 were statistically significant for DFA. Therefore, our results here  
456 demonstrated that hPSC-derived ONPs had greater tendency to cluster around  
457 DFA than EDA. All computed statistical values are shown in Supplementary  
458 Table S2.

459 To evaluate the direction of neurites of hPSC-derived ONPs, we first de-  
460 fined EDA in Region 1-3 ( $\phi'_j$ ,  $j = 1 - 3$ ) (Figure 10A) and DFA ( $\psi'_j$ ,  $j = 1 - 3$ );  
461 similarly defined  $\phi_i$  and  $\psi_i$  as in Figure 8. All of the EDAs and DFAs defined  
462 here can be found in Supplementary Table S3. Polar histograms of the neurite  
463 direction angle in Region 1–3 indicated that the two longest neurites were bi-  
464 modal in nature (Figure 10B). In contrast, polar histograms of those cultured  
465 with rhBDNF (negative control) and 800,000 PODS®-BNDF (positive control)  
466 did not indicate bimodal distribution—the neurites did not show directionality  
467 (Figure 10C). The Rayleigh test of uniformity for both the positive and negative  
468 control were greater than 0.05, demonstrating that both of the conditions had

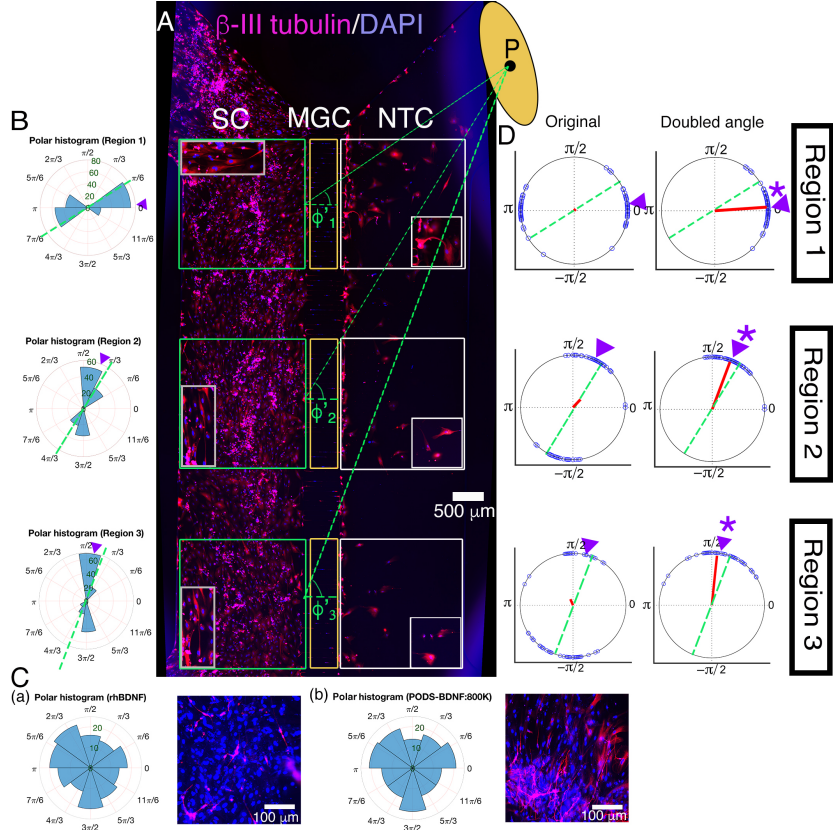


Figure 10: (A): Immunohistochemistry of hPSC-derived ONPs cultured in the Xona™ XC450 for seven days with  $\beta$ -III-Tubulin (pink fluorescence) and DAPI (blue fluorescence). A green line was drawn from the center of the BDNF disk (P) to the mid point of each of three pre-determined squares (Region 1–3) in the somal compartment to define Euclidean Distance Angle (EDA:  $\phi_i^c$ ,  $i = 1 - 3$ ). Green square: somal compartment (SC); yellow square: microgroove channels (MGC); White square: Neurotrophin compartment (NTC). High-power magnified images of the NTC and SC are shown. An ellipse-shaped PODS®-rhBDNF disc is shown in yellow. P: the center of the disk.(B): Polar histogram of neurite directional angles of hPSC-derived ONPs in the Xona™ XC450 at Day 7 (D7). The two longest neurites were measured. EDA: green dotted line. DFA: purple triangle. (C): (a) Right: Polar histogram of neurite directional angles of hPSC-derived ONPs cultured with 20 ng/mL of recombinant human BDNF for seven days. Left: Corresponding photomicrograph of immunocytochemistry with  $\beta$ -III tubulin (pink) and DAPI (blue). (b) Right: Polar histogram of neurite directional angles of hPSC-derived ONPs cultured with 800,000 of PODS®-rhBDNF for seven days. Left: Corresponding photomicrograph of immunocytochemistry with  $\beta$ -III tubulin (pink) and DAPI (blue). (D): A circular plot of neurite directional angle of hPSC-derived ONPs in Region 1–3. Once again, the two longest neurites were plotted on a unit circle. Right column: Original directional angle distribution. Left column: the method of doubling the angle applied to the original data. Each datum point is shown as a blue circle. Mean vector angle is shown as a red line. Green dotted line shows Euclidean Distance Angle (EDA) and purple triangle indicates Diffusion Flow Angle (DFA). \* symbol indicates that the mean vector angle fits within the 95% confidence internal ( $\alpha < 0.05$ .)

469 no statistically significant directionality (Supplementary Table S3: highlighted  
470 in green). We also analyzed the direction of the neurites using circular statistics.  
471 To obtain more realistic mean vector angles, we doubled each angle and reduced  
472 the multiples modulo 360°. In circular statistics, the bimodal distributed data  
473 can be transformed into a unimodal data by doubling the angle [32]. The mean  
474 vector angles in Figure 10D (right column) indicates the situation where the  
475 vectors were canceled out between the two groups of angles distributed in a bi-  
476 modal fashion, resulting in inaccurate representation. A circular plot in Figure  
477 10D (right column) showed doubled angles, representing actual representation  
478 of the neurite vector angles. In all of the three regions, the Reyleigh test and V  
479 test for EDA and DFA indicated directionality (Supplementary Table S3). One  
480 sample test for the mean vector angles in Region 1–3 indicated that they were  
481 not statistically different from DFA, but all of the three mean vector angles were  
482 statistically different from EDA.

483 We also stained the devices for  $\beta$ -III tubulin to track neurite growth and  
484 extension across the micro-groove channels as well as cell migration in three  
485 selected regions (Figure 10A). The location of the PODS®-rhBDNF disk in  
486 relation to the regions of interest in Figure 11A is indicated by a yellow circle.  
487 Quantitative analyses were performed and summarized in Figure 11B. Our data  
488 indicate that neurite length is dependent on BDNF concentration, with greater  
489 amounts of PODS®-rhBDNF promoting longer neurite growth (Figure 11B(a)).  
490 Lesser amounts of PODS®-rhBDNF, however, are necessary to create an ap-  
491 propriate concentration gradient. In the presence of 20,000 PODS®-rhBDNF,  
492 both neurite extension into the microchannels and cell migration into the neu-  
493 rotrophin compartment are greatest in the region closest to the BDNF source  
494 and decrease further from the PODS®-rhBDNF (Figure 11B(b,c)). Cell migra-  
495 tion is dependent on the distance from the source of BDNF, thus suggesting the  
496 presence of a BDNF gradient as predicted by our model. Note that the Xona  
497 microchannels intended to prevent from migration across channels.

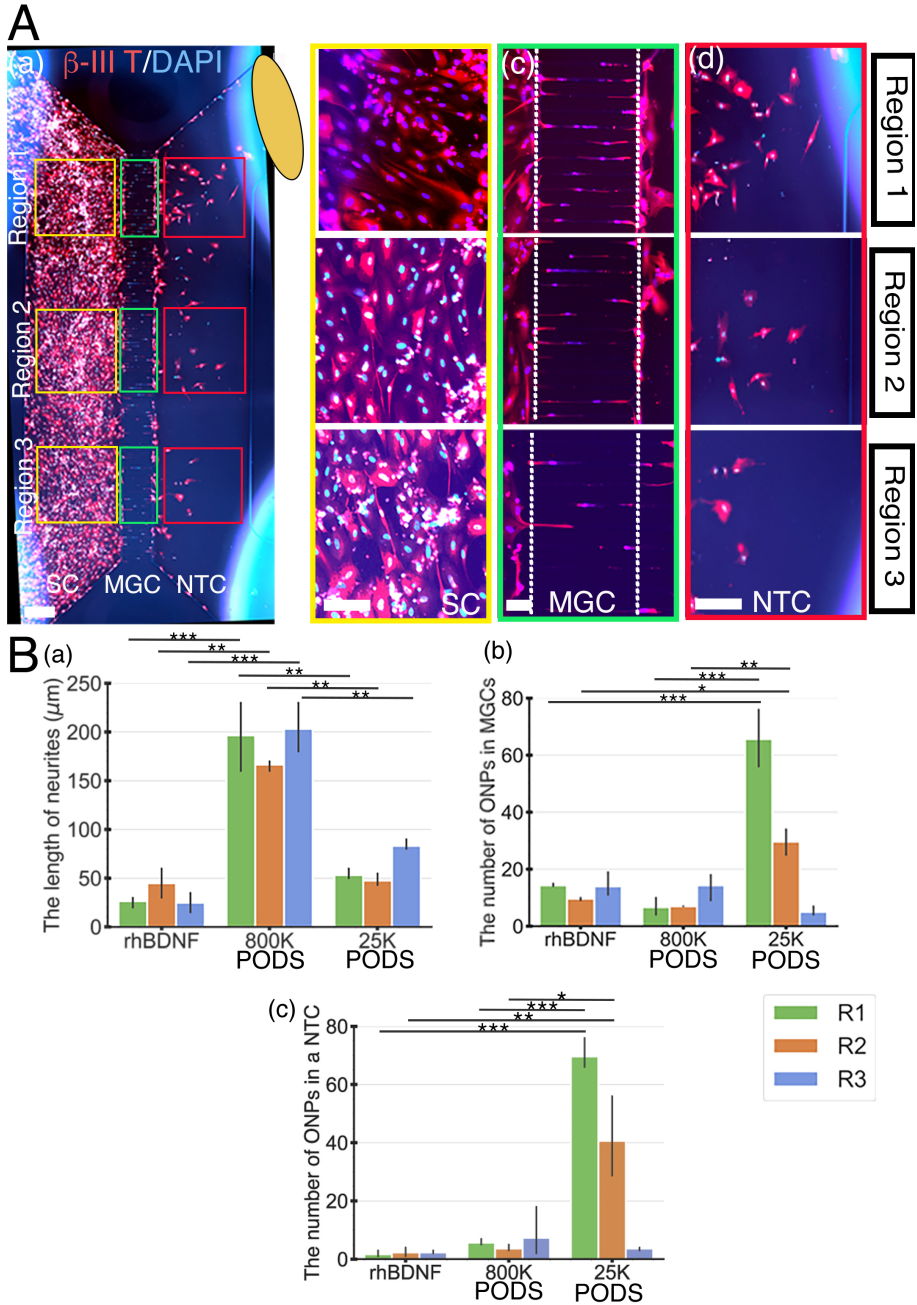


Figure 11: Human PSC-derived late-stage ONPs in the microfluidic device were stained with  $\beta$ -III tubulin (red) and DAPI (blue) to measure cell migration. (A): Late-stage ONPs stained after seven days in culture (a) with regions highlighted and magnified in the somal compartment (b), microgroove channels (c), and neurotrophin compartment (d). SC: somal compartment, MGC: microgroove channels, NTC: neurotrophic compartment. An ellipse-shaped PODS®-rhBDNF disc is shown in yellow. Scale bar (a): 500  $\mu\text{m}$ ; (b)–(d): 100  $\mu\text{m}$ . (B): Quantitative analyses of cell migration and neurite extension in devices using recombinant human BDNF, 800,000 PODS®-rhBDNF, or 20,000 PODS®-rhBDNF. \* :  $p < 0.05$ , \*\*:  $p < 0.01$ , \*\*\*:  $p < 0.001$ .

498     **4. Discussion**

499     *4.1. Challenges in neurotrophin treatment in the inner ear*

500     This is a proof-of-concept study for the realization of a neurotrophic strip  
501     to ascertain its scientific/technological parameters in a controlled *in vitro* en-  
502     vironment. Neurotrophin gradients have been studied for in multiple contexts  
503     [47, 48, 49]. However, it has not been feasible to reliably provide such a gra-  
504     dient to neurons neither *in vitro* nor *in vivo*, primarily because of technical  
505     challenges. While neurotrophin treatment has been recognized as a potential  
506     treatment for sensorineural hearing loss, there has not been clinical success in  
507     this avenue to date. Most recent relevant clinical trials used adeno-associated  
508     virus (AAV2) to deliver BDNF to the brain [50]. Although exciting, this treat-  
509     ment does not attempt to control the concentration of BDNF, which could  
510     potentially interfere with normal functions in a target organ [51]. Furthermore,  
511     this treatment may not be applicable to the inner ear. In this study, we used  
512     PODS®-rhBDNF to provide a neurotrophic gradient in a controlled fashion.  
513     Our result indicated 20,000 PODS-BDNF allowed for rhBDNF neurotrophin  
514     gradient such that hESC-derived ONPs survived, differentiated toward human  
515     SGNs, and also established directional neurite outgrowth in a microfluidic device.

516     *4.2. Microfluidic device-generated gradient*

517     We used a microfluidic device to advance our understanding of directional  
518     neurite growth and otic neuronal differentiation in response to a BDNF concen-  
519     tration gradient [52]. Among many *in vitro* concentration gradient sustaining  
520     culture devices, microfluidic devices have overcome many of the deficits that  
521     conventional platforms (i.e., the Boyden chamber, Dunn chambers, or compart-  
522     mentalized diffusion chambers) face [52]. Conventional platforms tend to be sub-  
523     optimal to manipulate small volumes of fluid at the order of microliters. Growth  
524     factors and proteins are used in minute amounts in our microfluidic device, and  
525     cultured stem cells are able to interact with endogenous factors. As mentioned  
526     earlier, this micro-environment more accurately represents *in vivo* conditions.

527 The Xona™ device can be used to sustain a three-dimensional concentration gra-  
528 dient over time (duration dependent on the half-life of the molecule) due to its  
529 microchannel array. The device limits convective flow in the gradient-forming  
530 areas by introducing microgroove channels that generate high fluidic resistance,  
531 thereby limiting flow to diffusion. The high resistance of the microchannel array  
532 also prolongs diffusion across them, thereby increasing both gradient formation  
533 and gradient steepness. These features allowed us to generate a FEM, which pre-  
534 dicted the necessary number of PODS®-BDNF crystals for a BDNF gradient.  
535 Note, however, that this environment is different from the micro environment  
536 in the inner ear. A mesh geometry of the cochlea will be needed to compute the  
537 PODS®-BDNF crystal number for our next step of this study.

538 *4.3. BDNF and Polyhedrin protein*

539 Over the course of past 20–30 years, it has been established that BDNF me-  
540 diates survival and differentiation activities on SGNs by binding and activating  
541 the tyrosine kinase receptor kinase B (TrkB), a member of the larger family  
542 of Trk receptors [20]. Numerous studies have reported that BDNF can palliate  
543 SGN degeneration in ototoxically deafened animals, a widely accepted model for  
544 retrograde trans-synaptic SGN degeneration secondary to hair cell destruction  
545 [13, 14, 53, 54]. Additionally, it has been confirmed that there is a positive corre-  
546 lation between SGN counts and CI performance [55]. It is then safe to presume  
547 that treating CI recipients with BDNF would enhance overall CI performance,  
548 by preserving SGNs and their neurites. However, simply introducing rhBDNF  
549 into the inner ear poses significant hurdles. Although promising, human BDNF  
550 treatment has not been currently implemented in the inner ear. Unsuccessful  
551 BDNF treatment can be explained by several factors [56].

552 The blood half-life of BDNF protein is extremely short, only 1–10 min in  
553 the plasma [57, 58] and one hour in CSF [59]. The BDNF's high degrada-  
554 tion rate would require continuous replenishment, impractical for clinical use.  
555 Furthermore, introduction of a homogeneous solution of BDNF would promote  
556 nondirectional neurite growth where directed neurite growth is essential for de-

signing our new-generation bioactive CI, as depicted in Figure 1A. Directing neurite growth towards the CI electrode array is pivotal in the ultimate goal of enhancing performance through the narrowing of the electrode-neuron gap. The PODS® system precludes the phenomena by its localized, gradual release of growth factor. The steady supply of BDNF from a localized origin not only creates a concentration gradient, but maintains it over time. As seen in Figures 4–6, we were able to perform a finite element analysis based on data we collected describing the chemical release kinetics and molar ratio of PODS®-BDNF system. It is clearly visible that the slow-release nature of PODS®-BDNF results in a concentration gradient over the course of Day 1–7 (Figure 5).

It should be noted that our FEM assumes free diffusion of the rhBDNF protein. In biological cell-culture conditions, BDNF released from PODS®-BDNF has tendency to adhere to the walls of the culture device because BDNF is a “sticky” protein of about 27 kDa (mature BDNF dimer) and it is positively charged under physiological conditions (isoelectric point, pI = 9.4) [60]. As such, the physio-chemical properties of BDNF have made the recombinant protein difficult to diffuse. This phenomenon was observable in preliminary data where the ONPs failed to survive past 1–3 days of culture (data not shown). To circumvent this issue we infused the culture media with a carrier protein (i.e., BSA), hypothesizing that the albumin would act as a carrier for the released BDNF and allow for free diffusion throughout the microfluidic device [61]. This hypothesis is supported by our sets of biological verification data (Figures 7–11) that clearly shows that hPSC-derived ONPs responded to the modification by exhibiting the expected cell body orientation, unidirectional neurite extension, and neurite length. Note that albumin is the single protein found in highest concentrations in the perilymph [62], therefore, a carrier protein will not be needed in our future *in vivo* study.

#### 4.4. Intracellular signaling initiated by Thyrosine kinase B receptor

Another issue we need to consider in interpretation of our results is the intracellular cell signaling mechanism elicited by rhBDNF. Human BDNF (mature

587 dimeric form) binds with high affinity to its TrkB receptor. The binding of  
588 BDNF to a TrkB receptor has proven to have significant importance for the  
589 proneuronal effects of BDNF [20]. Upon binding BDNF, TrkB dimerizes, and  
590 activates intrinsic kinase activities and other complex set of intracellular sig-  
591 naling cascades, which is beyond the scope of this study. However, it should  
592 be noted that activation of TrkB receptor by neurotrophin binding causes the  
593 TrkB protein to be internalized in endosomes on the cellular membrane [63].  
594 Endosomes can then be transported to the soma. Therefore, the proneuronal  
595 effects of rhBDNF in our results might have highly depended on the status of  
596 TrkB receptors on the cell membrane of hPSC-derived ONPs. Our previous  
597 study has demonstrated that strong expression of a TrkB receptor on derived  
598 ONPs [24], however, more detailed studies on TrkB receptors on hPSC-derived  
599 ONP and SGNs will be needed.

600 *4.5. Degradation of PODS® crystals by protease*

601 In cell culture, degradation of PODS®-rhBDNF is likely due to the activity  
602 of cell-secreted proteases. The proteases break down the peptide bonds of the  
603 encasing polyhedrin protein, creating openings in the structure to allow release  
604 of the rhBDNF. Therefore, the presence of proteases is imperative for the proper  
605 utilization of the PODS® crystals. Additionally, these proteases are responsible  
606 for the degradation of the released BDNF. Because stem cells are not present  
607 in the culture media used for the PODS® degradation kinetics experiments, we  
608 infused the media with 10% FBS, which naturally contains proteases, to promote  
609 polyhedrin degradation, BDNF release, and BDNF degradation to attain results  
610 that more accurately describe *in vitro* events. Moreover, since the cells and  
611 PODS are initially segregated into separate compartments within the culture  
612 device, cell-secreted proteases are unlikely to reach and degrade the PODS in  
613 time to support ONP survival and differentiation. Infusion of FBS was therefore  
614 required in these experiments as well. In clinical use, however, we presume  
615 that cell-secreted proteases will be readily present in the inner ear and would  
616 therefore preclude the need for artificial supplementation.

617     *4.6. A concept design: Neurotrophic strip*

618     The plateau in CI performance in treatment of sensorineural hearing loss has  
619     driven researchers to develop innovative supplementary treatment strategies to  
620     push the field past this hurdle. Our approach strives to directly address the  
621     issue at its core: the electrode-neuron gap, which can lead to serious implica-  
622     tions include low spatial frequency resolution and high power consumption. We  
623     can use our data as a launchpad for the neurotrophic strip (NS). The NS is a  
624     biointerface concept that integrates an extended-release source of growth factor  
625     to facilitate a protein gradient. Implanted in conjunction with the CI, it acts  
626     as a bridge between the extant SGNs and implanted late-ONPs grown on the  
627     electrode itself. The NS would promote survival of both cell populations, dif-  
628     ferentiation of the late ONP implants, promote directional neurite growth and  
629     synaptogenesis between the two, effectively creating a neuronal network between  
630     the patient and the implanted CI. Each electrode would be able to stimulate cell  
631     bodies at exceptionally high resolution, essential for greater intonation differ-  
632     entiability (required for effective social interaction and music appreciation) and  
633     so, increased quality of life for millions. Our successful outcomes are essential  
634     to make a neurotrophic strip feasible in *in vivo* environment.

635     *4.7. The limitations of this study and future direction*

636     There are some limitations associated with this study. First, the reduction of  
637     spacial dimension to 2D for diffusion modeling certainly affected the flux vector,  
638     which determines the predicted concentration vector. Given that the thickness  
639     (i.e., Z-axis) of the microfluidic device was 100  $\mu\text{m}$ , we estimated that the effect  
640     was minimal. In the future, we plan to use PSC-derived 3D spheroids in a somal  
641     compartment so that flux vector and concentration gradient vector can more  
642     accurately model the cell behavior. In this way, we will be able to circumvent  
643     the need to reduce diffusion calculations to 2D for computation performance in  
644     the modeling.

645     Secondly, we required to generate a model in that the BDNF's biological  
646     transportation phenomenon from a PODS<sup>®</sup>-rhBDNF disk to a somal compart-

647 ment of a Xona™ device. Note that in this model, we focused on the major  
648 dependent variable, BDNF concentration gradient to model the biological phe-  
649 nomenon. Other physical variables to promote cell migration, otic neuronal  
650 differentiation, and neurite growth were not take into consideration. These  
651 variables include electotaxis (electrical potential), durotaxis (matrix's stiffness  
652 [i.e., laminin 511 in our case]) [64], mechanotaxis (cell strain), and lastly cell  
653 migration by random walk [65]. In our future study, we will take these vari-  
654 ables into consideration to more accurately represent the migration and neurite  
655 growth of hPSC-derived ONPs.

656 Insufficient contrast between cells and background in phase contrast images  
657 led to inaccuracies in cell orientation computation for some images. To address  
658 this issue, poor quality images were disregarded in the quantitative analysis.  
659 We occasionally used manual measurement for accuracy. Our future study may  
660 entail automated time-series cell analysis, which would allow more accurate  
661 measurement. Also, another way to address this issue would be with a cell  
662 membrane staining in the future.

663 While 20,000 of PODS®-rhBDNF were necessary for hPSC-derived ONPs  
664 for otic neuronal differentiation and directional neurite outgrowth, this condi-  
665 tion may not be sufficient. For instance, it is still not known whether the effects  
666 of other neurotrophic factors such as Neurotrophin-3 and Glial cell line-derived  
667 neurotrophic factor could have a positive effect on ONP growth [20, 66, 67]. We  
668 are planning to investigate these neurotrophic factors in the future. Other fac-  
669 tors that could have an impact on directional neurite growth include endogenous  
670 factors secreted from hPSC-derived ONPs. While our previous study demon-  
671 strated that hPSC-derived ONPs only secreted negligible amount of BDNF that  
672 were detected by ELISA [9], currently we do not have any data on other neu-  
673 rotrophic factors or other molecules that could have affected directional neurite  
674 growth in the inner ear. We chose BDNF first to study because the most inten-  
675 sively studied neurotrophic factor in the field of hearing research is BDNF [20].  
676 Previous studies have indicated that neurotrophic supports of SGNs are mainly  
677 from BDNF and neurotrophin-3 (NT-3) [20, 60]. Therefore, the potential con-

678 founding effect of the secretions of other neurotrophic factors and molecules  
679 secreted from derived SGNs are likely NT-3, for which further investigation is  
680 necessary in the future.

681 Despite the aforementioned limitations associated in this study, the present  
682 results generated BDNF concentration gradient, condition of which is necessary  
683 for hPSC-derived ONPs to differentiate into the otic lineage (i.e., SGNs) and  
684 also promoted directional neurite extension towards the POD-BDNF disk. The  
685 technique will allow us to control neurite direction of transplanted hPSC-derived  
686 ONPs in the inner ear. We will harness this method in our design of a bioactive  
687 CI.

## 688 **Conclusions**

689 We were able to generate BDNF concentration gradient, enabling survival,  
690 neuronal differentiation toward SGNs, and directed neurite extension of hPSC-  
691 derived ONPs. The technique will allow us to control neurite direction of trans-  
692 planted hPSC-derived ONPs in the inner ear. This proof-of-concept study pro-  
693 vides a step toward next-generation bioactive CI technology.

## 694 **Acknowledgment**

695 This work was supported by the American Otological Society Clinician Sci-  
696 entist Award (AJM), the Triological Society/American College of Surgeons  
697 Clinician Scientist Award (AJM), the Department of Otolaryngology of North-  
698 western University (AJM), the NIH (NIDCD) K08 Clinician Scientist Award  
699 K08DC13829-02 (AJM), and the Office of the Assistant Secretary of Defense of  
700 Health Affairs through the Hearing Restoration Research Program (Award #:  
701 RH170013:WU81XWUH-18-0712). Imaging work was performed at the North-  
702 western University Center for Advanced Microscopy, which is generously sup-  
703 ported by NCI CCSG P30 CA060553 awarded to the Robert H. Lurie Com-  
704 prehensive Cancer Center, for which we thank Peter Dluhy, Constadina Ar-  
705 vanitis, Ph.D., David Kirchenbuechler, Ph.D., and Wensheng (Wilson) Liu,

706 M.D. Some of microfluidic device experiments were performed in the Analytical  
707 bioNanoTechnology (ANTEC) Core Facility of the Simpson Querrey Institute  
708 at Northwestern University, which is supported by the Soft and Hybrid Nan-  
709 otechnology Experimental (SHyNE) Resource (NSFECCS-1542205). We thank  
710 Shreyas Bharadwaj (Cornell University), Kyle Coots (Midwestern University),  
711 Andrew Oleksijew (the University of Nebraska), Duncan Chadly (California In-  
712 stitute of Technology), and Shun Kobayashi (the University of Texas at Austin)  
713 for their contribution to the earlier phases of this project. We thank Sara Dun-  
714 lop (Department of Neurology, Northwestern University), and Dr. Jacqueline  
715 Bond (the University of California San Diego) for assistance in Western Blot and  
716 SDS-Page gels. We also thank Dr. Georgia Minakaki (Department of Neurol-  
717 ogy, Northwestern University) on assistance in ELISA. Finally, our thanks and  
718 appreciation go to our collaborator, Dr. Christian Pernstich (Cell Guidance  
719 Systems), for continuous support and stimulating discussions on this project  
720 since 2015.

721 **References**

- 722 [1] J. G. Naples, M. J. Ruckenstein, Cochlear Implant., Otolaryngologic Clinics  
723 of North America 53 (1) (2020) 87–102. doi:10.1016/j.otc.2019.09.  
724 004.
- 725 [2] B. S. Wilson, M. F. Dorman, Cochlear implants: A remarkable past  
726 and a brilliant future, Hearing Research 242 (1-2) (2008) 3–21. arXiv:  
727 NIHMS150003, doi:10.1016/j.heares.2008.06.005.
- 728 [3] C. Frick, M. Müller, U. Wank, A. Tropitzsch, B. Kramer, P. Senn, H. Rask-  
729 Anderson, K. H. Wiesmüller, H. Löwenheim, Biofunctionalized peptide-  
730 based hydrogels provide permissive scaffolds to attract neurite outgrowth  
731 from spiral ganglion neurons, Colloids and Surfaces B: Biointerfaces 149  
732 (2017) 105–114. doi:10.1016/j.colsurfb.2016.10.003.

- 733 [4] S. Hahnewald, A. Tscherter, E. Marconi, J. Streit, H. R. Widmer, C. Gar-  
734 nham, H. Benav, M. Mueller, H. Löwenheim, M. Roccio, P. Senn, Response  
735 profiles of murine spiral ganglion neurons on multi-electrode arrays., Journal  
736 of neural engineering 13 (1) (2016) 16011. doi:10.1088/1741-2560/  
737 13/1/016011.
- 738 [5] R. K. Shepherd, S. Hatsushika, G. M. Clark, Electrical stimulation of  
739 the auditory nerve: The effect of electrode position on neural excitation,  
740 Hearing Research 66 (1) (1993) 108–120. doi:10.1016/0378-5955(93)  
741 90265-3.
- 742 [6] M. Tykocinski, L. T. Cohen, B. C. Pyman, T. Roland, C. Treaba, J. Palamara,  
743 M. C. Dahm, R. K. Shepherd, J. Xu, R. S. Cowan, N. L. Cohen,  
744 G. M. Clark, Comparison of electrode position in the human cochlea using  
745 various perimodiolar electrode arrays., The American journal of otology  
746 21 (2) (2000) 205–211. doi:10.1016/S0196-0709(00)80010-1.
- 747 [7] A. Roemer, U. Köhl, O. Majdani, S. Klöß, C. Falk, S. Haumann, T. Lenarz,  
748 A. Kral, A. Warnecke, Biohybrid cochlear implants in human neurosensory  
749 restoration., Stem cell research and therapy 7 (1) (2016) 148. doi:10.  
750 1186/s13287-016-0408-y.
- 751 [8] R. A. Heuer, K. T. Nella, H. T. Chang, K. S. Coots, A. M. Oleksijew,  
752 C. B. Roque, L. H. Silva, T. L. McGuire, K. Homma, A. J. Matsuoka,  
753 Three-dimensional otic neuronal progenitor spheroids derived from human  
754 embryonic stem cells, Tissue Engineering - Part A 27 (3-4) (2021) 256–269.  
755 doi:10.1089/ten.tea.2020.0078.
- 756 [9] H.-T. Chang, R. A. Heuer, A. M. Oleksijew, K. S. Coots, C. B. Roque, K. T.  
757 Nella, T. L. McGuire, A. J. Matsuoka, An Engineered Three-Dimensional  
758 Stem Cell Niche in the Inner Ear by Applying a Nanofibrillar Cellulose  
759 Hydrogel with a Sustained-Release Neurotrophic Factor Delivery System,  
760 Acta Biomaterialia 108 (2020) 111–127. doi:<https://doi.org/10.1016/j.actbio.2020.03.007>.

- 762 [10] L. Taylor, L. Jones, M. H. Tuszynski, A. Blesch, Neurotrophin-3 gradients  
763 established by lentiviral gene delivery promote short-distance axonal bridg-  
764 ing beyond cellular grafts in the injured spinal cord, *Journal of Neuroscience*  
765 26 (38) (2006) 9713–9721. doi:10.1523/JNEUROSCI.0734-06.2006.
- 766 [11] P. Senn, M. Roccio, S. Hahnwald, C. Frick, M. Kwiatkowska, M. Ishikawa,  
767 P. Bako, H. Li, F. Edin, W. Liu, H. Rask-Andersen, I. Pyykkö, J. Zou,  
768 M. Mannerström, H. Keppner, A. Homsy, E. Laux, M. Llera, J. P. Lel-  
769 louche, S. Ostrovsky, E. Banin, A. Gedanken, N. Perkas, U. Wank, K. H.  
770 Wiesmüller, P. Mistrík, H. Benav, C. Garnham, C. Jolly, F. Gander, P. Ul-  
771 rich, M. Müller, H. Löwenheim, NANOCI-Nanotechnology Based Cochlear  
772 Implant with Gapless Interface to Auditory Neurons, *Otology and Neuro-*  
773 *otology* 38 (8) (2017) e224—e231. doi:10.1097/MAO.0000000000001439.
- 774 [12] G. J. Goodhill, H. Baier, Axon Guidance: Stretching Gradients to  
775 the Limit, *Neural Computation* 10 (3) (1998) 521–527. doi:10.1162/  
776 089976698300017638.
- 777 [13] L. N. Gillespie, G. M. Clark, P. F. Bartlett, P. L. Marzella, BDNF-induced  
778 survival of auditory neurons *in vivo*: Cessation of treatment leads to ac-  
779 celerated loss of survival effects, *Journal of Neuroscience Research* 71 (6)  
780 (2003) 785–790. doi:10.1002/jnr.10542.
- 781 [14] L. N. Pettingill, R. L. Minter, R. K. Shepherd, Schwann cells geneti-  
782 cally modified to express neurotrophins promote spiral ganglion neuron  
783 survival *in vitro*, *Neuroscience* 152 (3) (2008) 821–828. doi:10.1016/j.  
784 *neuroscience*.2007.11.057. *Schwann*.
- 785 [15] R. K. Shepherd, A. Coco, S. B. Epp, Neurotrophins and electrical stim-  
786 ulation for protection and repair of spiral ganglion neurons following  
787 sensorineural hearing loss, *Hearing Research* 242 (2009) 100–109. doi:  
788 10.1016/j.heares.2007.12.005. *Neurotrophins*.
- 789 [16] B. Baseri, J. J. Choi, T. Deffieux, G. Samiotaki, Y. S. Tung, O. Olu-  
790 molade, S. A. Small, B. Morrison, E. E. Konofagou, Activation of sig-

- 791 naling pathways following localized delivery of systemically administered  
792 neurotrophic factors across the bloodbrain barrier using focused ultra-  
793 sound and microbubbles, Physics in Medicine and Biology 57 (7). doi:  
794 10.1088/0031-9155/57/7/N65.
- 795 [17] K. Ikeda, S. Nagaoka, S. Winkler, K. Kotani, H. Yagi, K. Nakanishi,  
796 S. Miyajima, J. Kobayashi, H. Mori, Molecular Characterization of Bom-  
797 byx mori Cytoplasmic Polyhedrosis Virus Genome Segment 4, Journal of  
798 Virology 75 (2) (2001) 988–995. doi:10.1128/jvi.75.2.988-995.2001.
- 799 [18] T. Suzuki, T. Kanaya, H. Okazaki, K. Ogawa, A. Usami, H. Watanabe,  
800 K. Kadono-Okuda, M. Yamakawa, H. Sato, H. Mori, S. Takahashi, K. Oda,  
801 Efficient protein production using a Bombyx mori nuclear polyhedrosis  
802 virus lacking the cysteine proteinase gene, Journal of General Virology  
803 78 (12) (1997) 3073–3080. doi:10.1099/0022-1317-78-12-3073.
- 804 [19] H. Mori, R. Ito, H. Nakazawa, M. Sumida, F. Matsubara, Y. Minobe,  
805 Expression of Bombyx mori cytoplasmic polyhedrosis virus polyhedrin in  
806 insect cells by using a baculovirus expression vector, and its assembly into  
807 polyhedra, Journal of General Virology 74 (1) (1993) 99–102. doi:10.  
808 1099/0022-1317-74-1-99.
- 809 [20] S. H. Green, E. Bailey, Q. Wang, R. L. Davis, The Trk A, B, C's of  
810 Neurotrophins in the Cochlea., Anatomical record (Hoboken, N.J. : 2007)  
811 295 (11) (2012) 1877–1895. doi:10.1002/ar.22587.
- 812 [21] I. Meyvantsson, D. J. Beebe, Cell culture models in microfluidic systems,  
813 Annual Review of Analytical Chemistry 1 (1) (2008) 423–449. doi:10.  
814 1146/annurev.anchem.1.031207.113042.
- 815 [22] Z.-J. Guo, M.-H. Yu, X.-Y. Dong, W.-L. Wang, T. Tian, X.-Y. Yu, X.-D.  
816 Tang, Protein composition analysis of polyhedra matrix of Bombyx mori  
817 nucleopolyhedrovirus (BmNPV) showed powerful capacity of polyhedra to  
818 encapsulate foreign proteins., Scientific reports 7 (1) (2017) 8768. doi:  
819 10.1038/s41598-017-08987-8.

- 820 [23] A. J. Matsuoka, Z. A. Sayed, N. Stephanopoulos, E. J. Berns, A. R. Wad-  
821 hwani, Z. D. Morrissey, D. M. Chadly, S. Kobayashi, A. N. Edelbrock,  
822 T. Mashimo, C. A. Miller, T. L. McGuire, S. I. Stupp, J. A. Kessler,  
823 Creating a stem cell niche in the inner ear using self-assembling peptide  
824 amphiphiles., Plos One 12 (12) (2017) e0190150. doi:10.1371/journal.  
825 pone.0190150.
- 826 [24] A. J. Matsuoka, Z. D. Morrissey, C. Zhang, K. Homma, A. Belmadani,  
827 C. A. Miller, D. M. Chadly, S. Kobayashi, A. N. Edelbrock, M. Tanaka-  
828 Matakatsu, D. S. Whitlon, L. Lyass, T. L. McGuire, S. I. Stupp, J. A.  
829 Kessler, Directed Differentiation of Human Embryonic Stem Cells Toward  
830 Placode-Derived Spiral Ganglion-Like Sensory Neurons, Stem Cells Trans-  
831 lational Medicine 6 (2017) 923–936. doi:10.1002/sctm.16-0032.
- 832 [25] H. Al-Ali, S. R. Beckerman, J. L. Bixby, V. P. Lemmon, In vitro models  
833 of axon regeneration, Experimental Neurology 287 (Pt 3) (2017) 423–434.  
834 doi:10.1016/j.expneurol.2016.01.020.
- 835 [26] U. K. Laemmli, Cleavage of structural proteins during the assembly of  
836 the head of bacteriophage T4., Nature 227 (5259) (1970) 680–685. doi:  
837 10.1038/227680a0.
- 838 [27] A. L. Mandel, H. Ozdener, V. Utermohlen, Identification of pro- and mature  
839 brain-derived neurotrophic factor in human saliva., Archives of oral biology  
840 54 (7) (2009) 689–695. doi:10.1016/j.archoralbio.2009.04.005.
- 841 [28] C. A. Schneider, W. S. Rasband, K. W. Eliceiri, NIH Image to ImageJ:  
842 25 years of image analysis, Nature Methods 9 (7) (2012) 671–675. arXiv:  
843 arXiv:1011.1669v3, doi:10.1038/nmeth.2089.
- 844 [29] R. W. Burry, Controls for immunocytochemistry: an update., The journal  
845 of histochemistry and cytochemistry : official journal of the Histochemistry  
846 Society 59 (1) (2011) 6–12. doi:10.1369/jhc.2010.956920.

- 847 [30] M. B. Mazalan, M. A. B. Ramlan, J. H. Shin, T. Ohashi, Effect of geomet-  
848 ric curvature on collective cell migration in tortuous microchannel devices,  
849 *Micromachines* 11 (7) (2020) 1–17. doi:10.3390/MI11070659.
- 850 [31] F. Xu, T. Beyazoglu, E. Hefner, U. A. Gurkan, U. Demirci, Automated  
851 and adaptable quantification of cellular alignment from microscopic images  
852 for tissue engineering applications, *Tissue Engineering - Part C: Methods*  
853 17 (6) (2011) 641–649. doi:10.1089/ten.tec.2011.0038.
- 854 [32] E. Batschelet, *Circular Statistics in Biology* (Mathematics in Biology Series),  
855 1st Edition, Academic Press, New York, NY, 1981.
- 856 [33] P. Berens, M. J. Velasco, CircStat for Matlab: Toolbox for circular statistics  
857 with Matlab, Max–Planck–Institut f ur biologische Kybernetik, Technical  
858 Report No. 184 31 (10) (2009) 1–21. doi:doi:10.18637/jss.v031.i10.
- 859 [34] M. Pool, J. Thiemann, A. Bar-Or, A. E. Fournier, NeuriteTracer: A novel  
860 ImageJ plugin for automated quantification of neurite outgrowth, *Journal*  
861 of Neuroscience Methods 168 (1) (2008) 134–139. doi:10.1016/j.  
862 jneumeth.2007.08.029.
- 863 [35] E. Meijering, M. Jacob, J.-C. F. Sarria, P. Steiner, H. Hirling, M. Unser,  
864 Design and validation of a tool for neurite tracing and analysis in fluo-  
865 rescence microscopy images., *Cytometry. Part A : the journal of the Inter-  
866 national Society for Analytical Cytology* 58 (2) (2004) 167–176. doi:  
867 10.1002/cyto.a.20022.
- 868 [36] M. Anniko, W. Arnold, T. Stigbrand, A. Strom, The Human Spiral Gan-  
869 glion, *ORL* 57 (1995) 68–77.
- 870 [37] S. van der Walt, S. C. Colbert, G. Varoquaux, The NumPy Array: A  
871 Structure for Efficient Numerical Computation, *Computing in Science En-  
872 gineering* 13 (2) (2011) 22–30. doi:10.1109/MCSE.2011.37.
- 873 [38] J. D. Hunter, Matplotlib: A 2D Graphics Environment, *Computing in  
874 Science Engineering* 9 (3) (2007) 90–95. doi:10.1109/MCSE.2007.55.

- 875 [39] P. Virtanen, R. Gommers, T. E. Oliphant, M. Haberland, T. Reddy,  
876 D. Cournapeau, E. Burovski, P. Peterson, W. Weckesser, J. Bright, S. J.  
877 van der Walt, M. Brett, J. Wilson, K. J. Millman, N. Mayorov, A. R. J.  
878 Nelson, E. Jones, R. Kern, E. Larson, C. J. Carey, I. Polat, Y. Feng,  
879 E. W. Moore, J. VanderPlas, D. Laxalde, J. Perktold, R. Cimrman, I. Hen-  
880 riksen, E. A. Quintero, C. R. Harris, A. M. Archibald, A. H. Ribeiro,  
881 F. Pedregosa, P. van Mulbregt, SciPy 1.0: fundamental algorithms for  
882 scientific computing in Python., *Nature methods* 17 (3) (2020) 261–272.  
883 doi:10.1038/s41592-019-0686-2.
- 884 [40] P. Berens, CircStat : A MATLAB Toolbox for Circular Statistics , *Journal*  
885 *of Statistical Software* 31 (10). doi:10.18637/jss.v031.i10.
- 886 [41] M. Tuncel, H. S. Sürkü, K. M. Erbil, A. Konan, Formation of the cochlear  
887 nerve in the modiolus of the guinea pig and human cochleae., *Archives of*  
888 *medical research* 36 (5) (2005) 436–40. doi:10.1016/j.arcmed.2005.02.  
889 003.
- 890 [42] B. Küçük, K. Abe, T. Ushiki, Y. Inuyama, S. Fukuda, Kazuo Ishikawa,  
891 Microstructures of the Bony Modiolus in the Human Cochlea : A Scanning  
892 Electron Microscopic Study, *Journal of Electron Microsc* 40 (40) (1991)  
893 193–197.
- 894 [43] O. Levenspiel, *Chemical Reaction Engineering*, 3rd Edition, John Wiley  
895 and Sons, Inc., New York, NY, 1999.
- 896 [44] M. Stroh, W. R. Zipfel, R. M. Williams, S. C. Ma, W. W. Webb, W. M.  
897 Saltzman, Multiphoton microscopy guides neurotrophin modification with  
898 poly(ethylene glycol) to enhance interstitial diffusion, *Nature Materials*  
899 3 (7) (2004) 489–494. doi:10.1038/nmat1159.
- 900 [45] S. Axler, *Linear Algebra Done Right*, 3rd Edition, Springer Publishing,  
901 New York, NY, 2015.

- 902 [46] J. Crank, The mathematics of Diffusion, 2nd Edition, Oxford University  
903 Press, London, UK, 1979.
- 904 [47] K. M. Keefe, I. S. Sheikh, G. M. Smith, Targeting Neurotrophins to Specific  
905 Populations of Neurons: NGF, BDNF, and NT-3 and Their Relevance  
906 for Treatment of Spinal Cord Injury., International journal of molecular  
907 sciences 18 (3). doi:10.3390/ijms18030548.
- 908 [48] B. I. Awad, M. A. Carmody, M. P. Steinmetz, Potential role of growth  
909 factors in the management of spinal cord injury., World Neurosurgery 83 (1)  
910 (2015) 120–131. doi:10.1016/j.wneu.2013.01.042.
- 911 [49] E. R. n. Hollis, M. H. Tuszynski, Neurotrophins: potential therapeutic tools  
912 for the treatment of spinal cord injury., Neurotherapeutics : the journal of  
913 the American Society for Experimental NeuroTherapeutics 8 (4) (2011)  
914 694–703. doi:10.1007/s13311-011-0074-9.
- 915 [50] A. H. Nagahara, B. R. Wilson, I. Ivasyk, I. Kovacs, S. Rawalji, J. R.  
916 Bringas, P. J. Piviroto, W. S. Sebastian, L. Samaranch, K. S. Bankiewicz,  
917 M. H. Tuszynski, MR-guided delivery of AAV2-BDNF into the entorhi-  
918 nal cortex of non-human primates., Gene therapy 25 (2) (2018) 104–114.  
919 doi:10.1038/s41434-018-0010-2.
- 920 [51] S. D. Croll, C. Suri, D. L. Compton, M. V. Simmons, G. D. Yan-  
921 copoulos, R. M. Lindsay, S. J. Wiegand, J. S. Rudge, H. E. Scharfman,  
922 Brain-derived neurotrophic factor transgenic mice exhibit passive avoid-  
923 ance deficits, increased seizure severity and in vitro hyperexcitability in  
924 the hippocampus and entorhinal cortex., Neuroscience 93 (4) (1999) 1491–  
925 1506. doi:10.1016/s0306-4522(99)00296-1.
- 926 [52] A. Dravid, S. Parittotokkaporn, Z. Aqrawe, S. J. O'Carroll, D. Svirskis,  
927 Determining Neurotrophin Gradients in Vitro to Direct Axonal Outgrowth  
928 following Spinal Cord Injury, ACS Chemical Neuroscience 11 (2) (2020)  
929 121–132. doi:10.1021/acschemneuro.9b00565.

- 930 [53] T. Yamagata, J. M. Miller, M. Ulfendahl, N. P. Olivius, R. A. Altschuler,  
931 I. Pyykkö, G. Bredberg, Delayed neurotrophic treatment preserves nerve  
932 survival and electrophysiological responsiveness in neomycin-deafened  
933 guinea pigs., *Journal of neuroscience research* 78 (1) (2004) 75–86. doi:  
934 10.1002/jnr.20239.
- 935 [54] M. P. Zanin, M. Hellstr??m, R. K. Shepherd, A. R. Harvey, L. N. Gillespie,  
936 Development of a cell-based treatment for long-term neurotrophin expres-  
937 sion and spiral ganglion neuron survival, *Neuroscience* 277 (2014) 690–699.  
938 doi:10.1016/j.neuroscience.2014.07.044.
- 939 [55] M. Seyyedi, L. Viana, J. J. Nadol, Within-subject comparison of word  
940 recognition and spiral ganglion cell count in bilateral cochlear implant  
941 recipients, *Otol Neurotol* 35 (8) (2014) 1446–1450. doi:10.1097/MAO.  
942 000000000000443.Within-Subject.
- 943 [56] A. Henriques, C. Pitzer, A. Schneider, Neurotrophic growth factors for the  
944 treatment of amyotrophic lateral sclerosis: where do we stand?, *Frontiers*  
945 in neuroscience 4 (2010) 32. doi:10.3389/fnins.2010.00032.
- 946 [57] J. F. Poduslo, G. L. Curran, Permeability at the blood-brain and  
947 blood-nerve barriers of the neurotrophic factors: NGF, CNTF, NT-3,  
948 BDNF, *Molecular Brain Research* 36 (2) (1996) 280–286. doi:10.1016/  
949 0169-328X(95)00250-V.
- 950 [58] T. Sakane, W. M. Pardridge, Carboxyl-directed pegylation of brain-derived  
951 neurotrophic factor markedly reduces systemic clearance with minimal loss  
952 of biologic activity (1997). doi:10.1023/A:1012117815460.
- 953 [59] R. G. Soderquist, E. D. Milligan, E. M. Sloane, J. A. Harrison, K. K.  
954 Douvas, J. M. Potter, T. S. Hughes, R. A. Chavez, K. Johnson, L. R.  
955 Watkins, M. J. Mahoney, PEGylation of brain-derived neurotrophic factor  
956 for preserved biological activity and enhanced spinal cord distribution.,  
957 *Journal of biomedical materials research. Part A* 91 (3) (2009) 719–729.  
958 doi:10.1002/jbm.a.32254.

- 959 [60] M. Sasi, B. Vignoli, M. Canossa, R. Blum, Neurobiology of local and inter-  
960 cellular BDNF signaling, *Pflugers Archiv : European journal of physiology*  
961 469 (5-6) (2017) 593–610. doi:10.1007/s00424-017-1964-4.
- 962 [61] X. Li, Y. Su, S. Liu, L. Tan, X. Mo, S. Ramakrishna, Encapsulation  
963 of proteins in poly(l-lactide-co-caprolactone) fibers by emulsion electro-  
964 spinning, *Colloids and Surfaces B: Biointerfaces* 75 (2) (2010) 418–424.  
965 doi:10.1016/j.colsurfb.2009.09.014.
- 966 [62] E. E. L. Swan, M. Peppi, Z. Chen, K. M. Green, J. E. Evans, M. J.  
967 McKenna, M. J. Mescher, S. G. Kujawa, W. F. Sewell, Proteomics analysis  
968 of perilymph and cerebrospinal fluid in mouse., *The Laryngoscope* 119 (5)  
969 (2009) 953–958. doi:10.1002/lary.20209.
- 970 [63] T. Numakawa, S. Suzuki, E. Kumamaru, N. Adachi, M. Richards,  
971 H. Kunugi, BDNF function and intracellular signaling in neurons, *Histology  
and Histopathology* 25 (2) (2010) 237–258. doi:10.14670/HH-25.237.
- 973 [64] C. Gentile, Engineering of Spheroids for Stem Cell Technology, *Current  
974 Stem Cell Research & Therapy* 11 (2016) 652–665. doi:10.2174/  
975 1574888x10666151001114848.
- 976 [65] H. Berg, *Random Walks in Biology*, Princeton Universtiyy Press, Prinston,  
977 NJ, 1983.
- 978 [66] H. Li, F. Edin, H. Hayashi, O. Gudjonsson, N. Danckwardt-Lillies, H. En-  
979 gqvist, H. Rask-Andersen, W. Xia, Guided growth of auditory neurons:  
980 Bioactive particles towards gapless neural electrode interface, *Biomaterials*  
981 122 (2017) 1–9. doi:10.1016/j.biomaterials.2016.12.020.
- 982 [67] J. Schulze, H. Staeker, D. Wedekind, T. Lenarz, A. Warnecke, Expression  
983 pattern of brain-derived neurotrophic factor and its associated receptors:  
984 Implications for exogenous neurotrophin application., *Hearing Research* 413  
985 (2020) 108098. doi:10.1016/j.heares.2020.108098.